

Fast rotatation analysis of the Run–1 End–game data set with the Cornell Fourier method

A. Chapelain¹, J. Fagin¹, D. Rubin¹, and D. Seleznev¹

¹Cornell University

Abstract

This note presents the details of the reconstruction of the muon beam radial distribution of the Run–1 End–game data set with the Cornell fast rotation Fourier method. The radial distribution is used to estimate the electric field correction to the anomalous spin precession frequency of the muon ω_a .

Contents

1	Introduction	2
2	Data set	3
3	Fast Rotation signal	4
3.1	Positron counts histogram	4
3.2	Combination of the 24 calorimeters	4
3.3	Wiggle fit	4
3.4	Fast rotation signal	5
4	Nominal analysis	8
4.1	Choice of the t_s parameter	8
4.2	Choice of the t_m parameter	9
4.3	Choice of the t_0 parameter	9
4.4	Frequency distribution	9
4.5	Radial distribution	9
4.6	Electric field correction estimation	10
5	Per-calorimeter and per-bunch analysis	16

5.1	Per-calorimeter analysis	16
5.2	Per-bunch analysis	21
6	Statistical uncertainty	24
6.1	Nominal analysis	24
6.2	Per-bunch analysis	24
6.3	Per-calorimeter analysis	25
7	Systematic uncertainties	30
7.1	t_0 systematic	30
7.2	t_s systematic	32
7.3	t_m systematic	37
7.4	Frequency interval	43
7.5	Background	46
7.5.1	Background definition	46
7.5.2	Background removal	47
7.6	Wiggle fit	50
7.7	Positron energy threshold	52
7.8	Summary	54
8	Conclusion	54
A	Fast rotation histogram per-bunch	57
B	Fast rotation histogram per-calorimeter	57
C	Wiggle fit residuals	57
D	Fast rotation histogram for different positron energy thresholds	57

1 Introduction

This note presents the reconstruction of the radial distribution of the muon beam for the Run–1 End–game data set with the Cornell fast rotation Fourier analysis. The details of the Cornell fast rotation Fourier analysis are presented in [1] and the study of its performance with toy Monte Carlo simulations presented in [2]. More details about the Cornell fast rotation Fourier method can be found in [3, 4]. The analysis code’s user guide can be found in [5]. The fast rotation Fourier method aims at reconstructing the radial distribution of the stored

muon beam, via reconstructing the frequency distribution, in order to estimate the electric field correction C_E to the anomalous spin precession frequency of the muon ω_a . The electric field correction can be estimated in first approximation with the following formula:

$$C_E = \frac{\Delta\omega_a}{\omega_a} = -2n(1-n)\beta^2 \frac{\langle x_e^2 \rangle}{R_0^2}, \quad (1)$$

where

$$\langle x_e^2 \rangle = x_e^2 + \sigma^2, \quad (2)$$

where x_e is the equilibrium radius (average radial position) and σ the radial width of the beam, R_0 is the magic radius of 7112 mm, β the relativistic speed, and n the field index that relates to the electrostatic quadrupole electric field gradient like:

$$n = \frac{m\gamma r}{pB_0} \frac{\partial E_r}{\partial r}, \quad (3)$$

where m is the mass, γ the Lorentz factor, r the radial distance from the center of the storage ring, p the momentum, and E_r the radial component of the quadrupole electric field.

The ultimate goal of the Fermilab E–989 experiment is an uncertainty budget on the electric field correction of 20 ppb. This uncertainty translates into knowing both the average and the width of the cyclotron revolution frequency distribution to couple 0.1 kHz, which corresponds to knowing both the equilibrium radius and the width of the radial distribution to couple 0.1 mm. The electric field correction uncertainty budget for the Run–1 data set is not as stringent given the anticipated statistical and systematic uncertainties on ω_a of hundreds of ppb. A total uncertainty of 50 ppb on the electric field correction for the Run–1 data set would reach enough precision.

The reader is expected to be familiar with [1] and [2] before reading further this analysis note.

2 Data set

The data set being analyzed in this note is the Fermilab E–989 Run–1 End–game data set. The version of the reconstructed data set used in this analysis and provided by the production team is [6]:

```
gm2pro_daq_full_run1_EndGame_5039A_goldList.
```

The full data quality (fill-by-fill, subrun-by-subrun including the magnetic field information) is applied. The relevant information to the fast rotation analysis is obtained from the Recon West data products.

3 Fast Rotation signal

The details regarding how to produce the fast rotation signal can be found in [1] Sec. 3.

3.1 Positron counts histogram

The input to the fast rotation analysis is the same as the input to the anomalous spin precession frequency analysis: a histogram of the positron counts versus the time in the fill. This histogram was produced for each of the 24 calorimeters, and for each of the 8 bunches in the accelerator cycle. The nominal value of the positron energy threshold is 1,500 MeV. The choice of the energy threshold will be a source of systematic uncertainty (see Sec. 7.7).

3.2 Combination of the 24 calorimeters

The positron counts histograms of the 24 calorimeters are merged together for the nominal analysis (the 8 accelerator bunches are merged together for each calorimeter) The histograms from calorimeters #2 to #24 are added to the histogram of calorimeter #1 (taken arbitrarily as the reference) time shifting them by $(\# - 1) \times T_c/24$ where $\#$ is the calorimeter number and T_c the nominal cyclotron period of 149.14 ns corresponding to the so-called “magic momentum”. The value of the cyclotron period is updated to the measured value after completing the first round of the analysis and the analysis is performed again. The small variation of the cyclotron frequency results in a small variation of the time shift constant (well below the ns level) and therefore yields a negligible change in the fast rotation results. Figure 1 shows the positron counts histogram for all the 24 calorimeters combined. The time interval of the histogram is 1 ns. The analysis is also performed per calorimeter and per bunch as presented in 5.

3.3 Wiggle fit

It is necessary to fit the positron counts histogram in order to factor out at the very least the muon life-time (exponential decay). Section 7.6 will show that the results change little fitting for more than the muon life-time. The default fit is the 9-parameter fit that includes the muon life-time, anomalous spin precession and CBO modulation:

$$N(t) = N_0 \cdot e^{-t/\tau_\mu} [1 + A \cdot \cos(\omega_a t + \phi)] \cdot e^{-t/\tau_{cbo}} [1 + A_{cbo} \cdot \cos(\omega_{cbo} t + \phi_{cbo})], \quad (4)$$

where N_0 is the number of detected positron at $t = 0$, τ_μ is the muon boosted life-time of about 64 μs , A called the asymmetry is the amplitude of the anomalous spin precession modulation, ω_a the anomalous spin precession frequency (or spin tune), ϕ the phase of the

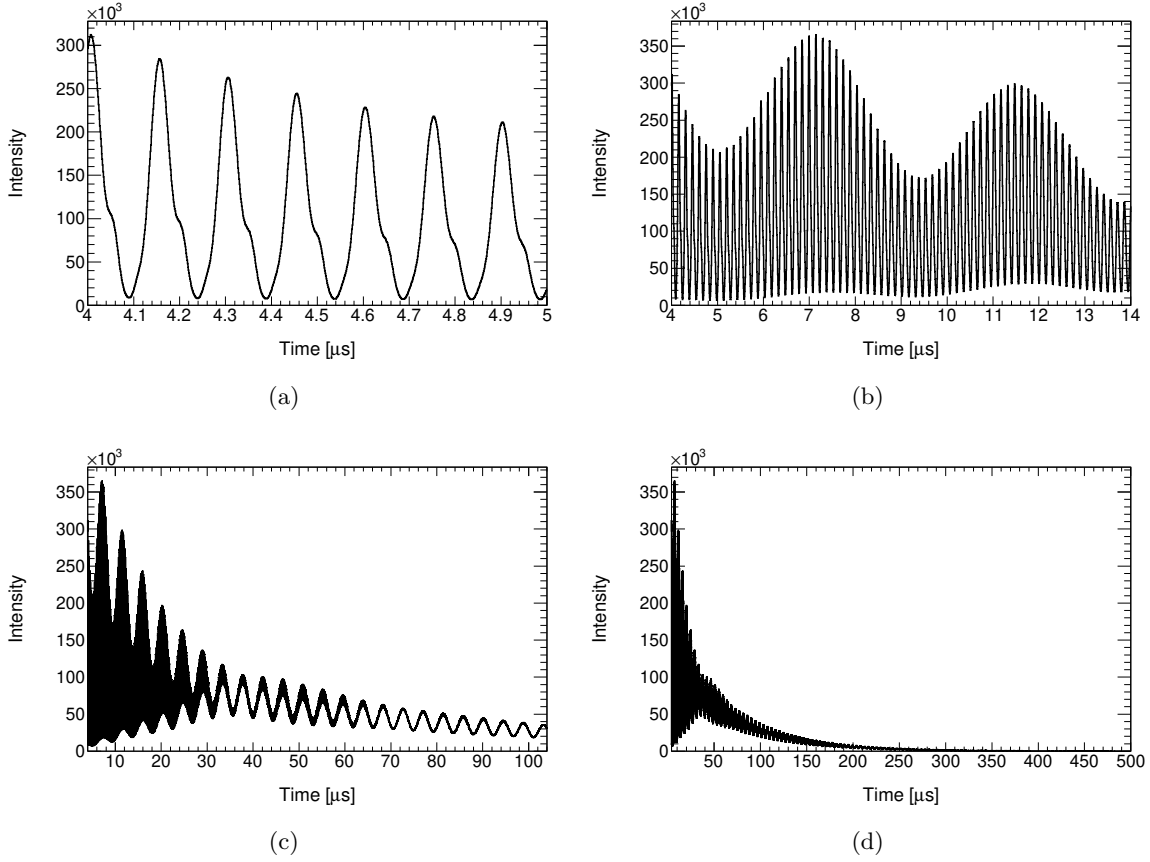


Figure 1: Positron counts as a function of time as seen by all the calorimeters combined for the Run–1 End–game data set for the time ranges: (a) 4–5, (b) 4–14, (d) 4–104 and (e) 4–500 μs with respect to the beam injection. The time interval is 1 ns.

modulation, τ_{cbo} the CBO life-time, A_{cbo} the amplitude of the CBO modulation, ω_{cbo} the frequency of the CBO modulation, and ϕ_{cbo} the phase of the modulation.

Figure 2 shows the fit of the positron counts histogram starting at 30 μs with respect to the beam injection. The histogram was re-binned to a time interval of 149 ns to average out in good approximation the fast rotation feature. Appendix C shows the fit residuals for different time ranges.

3.4 Fast rotation signal

The fast rotation signal is obtained by dividing out the fit function, given proper normalization to account for the 1 ns versus 149 ns time intervals, from the original positron counts histogram. Figure 3 shows the fast rotation signal for different time ranges. The appendices A and B show the various fast rotation histograms for each calorimeter and each bunch.

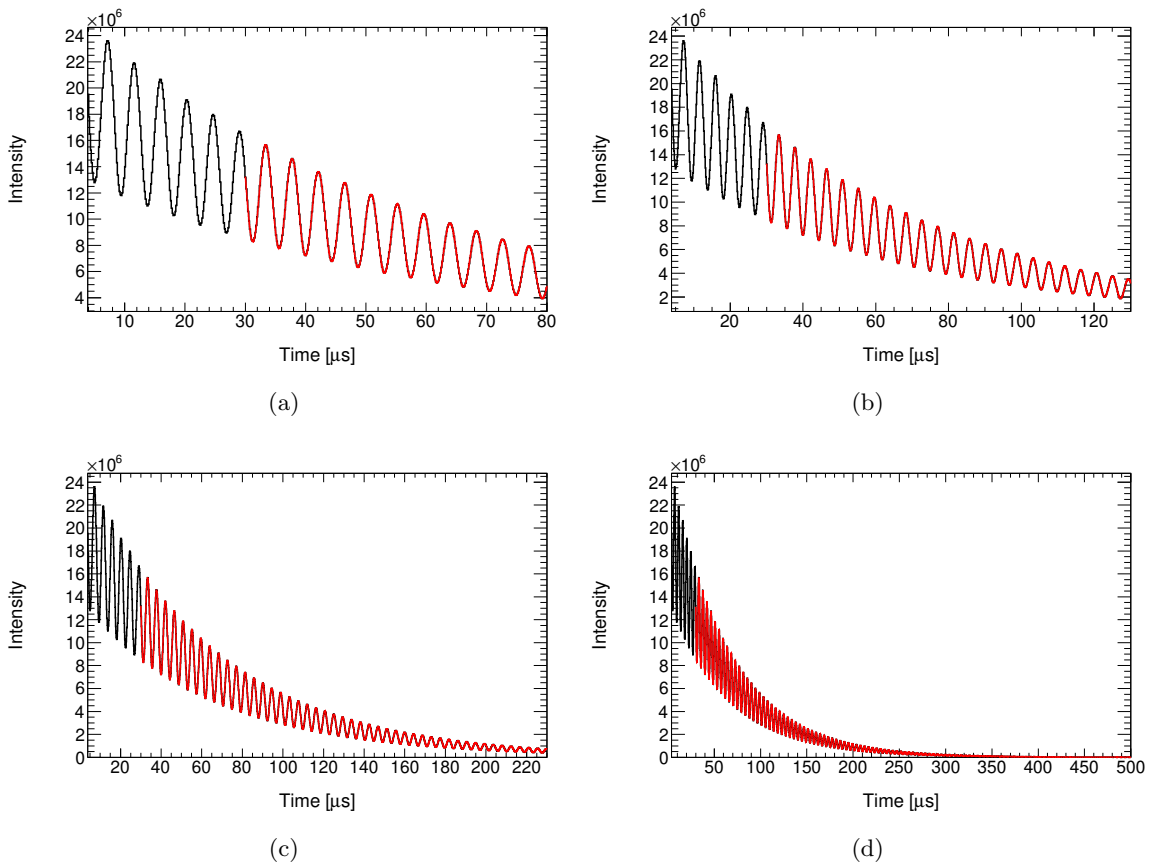


Figure 2: Fit of the positron counts histogram as a function of time as seen by all the calorimeters combined for the Run-1 End-game data set for the time ranges: (a) 4-80, (b) 4-130, (d) 4-230 and (e) 4-500 μs with respect to the beam injection. The time interval is 149 ns.

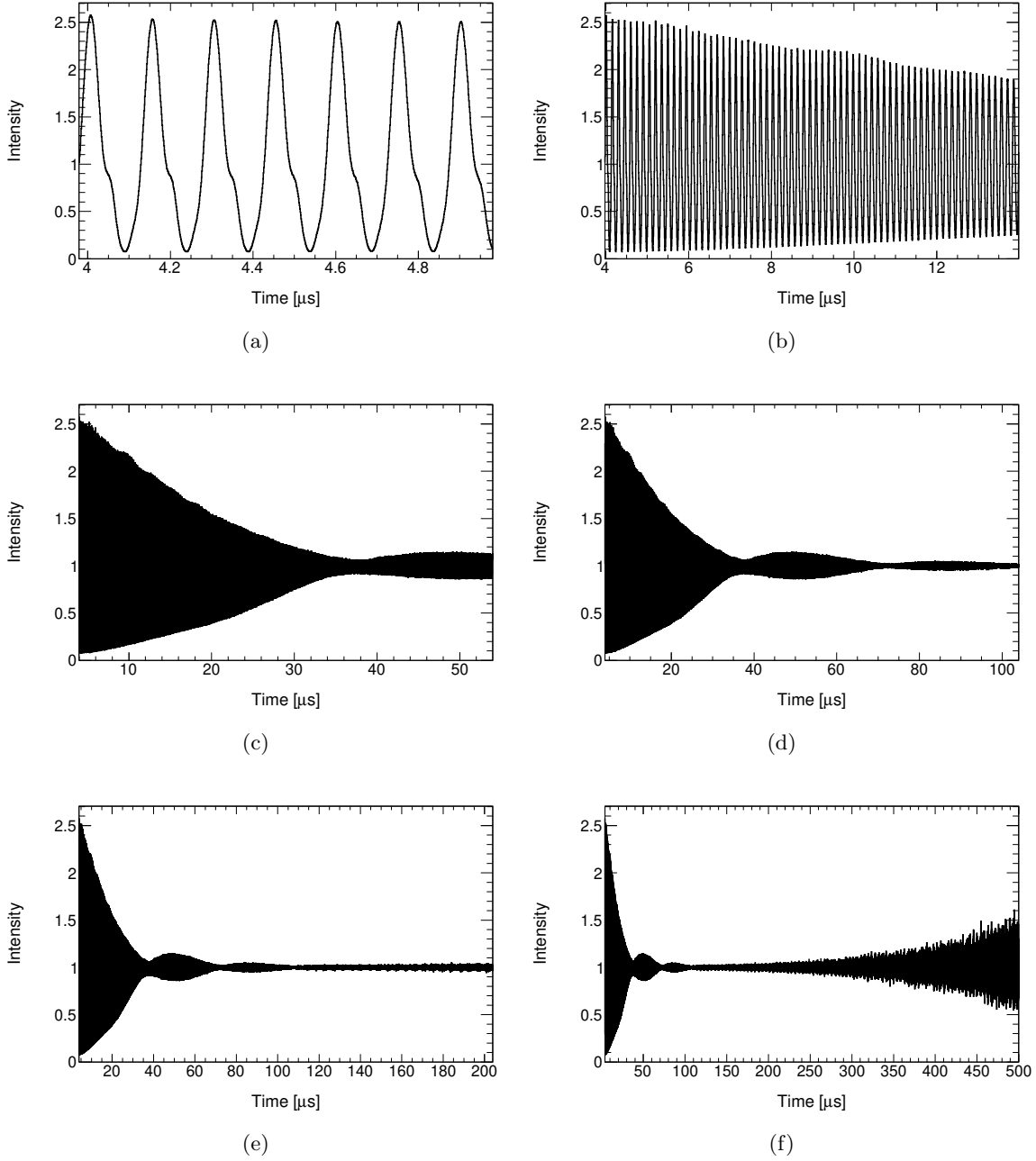


Figure 3: Fast rotation signal as a function of time as seen by all the calorimeters combined for the Run-1 End-game data set for the time ranges: (a) 4-5, (b) 4-14, (d) 4-54, (e) 4-104, (f) 4-204 and (g) 4-504 μs with respect to the beam injection. The time interval is 1 ns. The modulation with a 35 μs period corresponds to the beam partially and slowly re-bunching due to its asymmetric momentum distribution. This could potentially also be a sign of time-momentum correlation in the incoming beam profile.

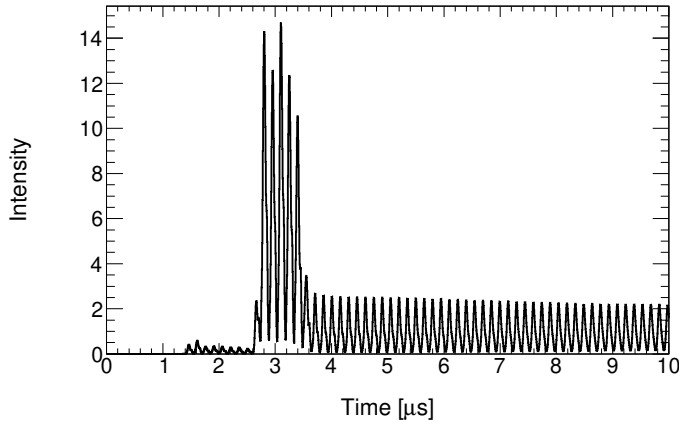


Figure 4: Fast rotation signal as a function of time as seen by all the calorimeters combined for the Run–1 End–game data set for the time ranges $0\text{--}10 \mu\text{s}$ with respect to the beam injection. The time interval is 1 ns.

4 Nominal analysis

This section will detail the nominal analysis of the Run–1 End–game data set. Section 6 and 7 will present respectively the statistical and systematic uncertainties estimation. The details of the analysis can be found in [1].

4.1 Choice of the t_s parameter

The t_s parameter is the start time of the analysis. The ideal case would be $t_s = t_0$ where t_0 corresponds to the time when the centroid of the longitudinal profile of the beam is detected by calorimeter #1 right after injection (first turn of the beam into the ring). This ideal scenario is unfortunately not possible for two reasons. The first is the saturation of the calorimeter electronics during the first μs of the fill due to the high intensity of the incoming beam. The second is the contamination by beam-line positrons of the incoming muon beam. The positrons are lost due to synchrotron radiation after about $3\text{--}4 \mu\text{s}$. Figure 4 shows the fast rotation signal for the first $10 \mu\text{s}$. The first μs is not available due to the saturation, and the signal stabilizes at $3\text{--}4 \mu\text{s}$ after the positrons are lost. The t_s value, because of the reasons explained above, is set to $t_s = 4 \mu\text{s}$. This value is slightly optimized such as the optimized t_s value corresponds to the fast rotation signal intensity of 1. This is done in order to minimize the effect from spectral leakage (see [1] Sec. 7.1 and 7.2). The optimized value is $t_s = 3.9765 \mu\text{s}$.

4.2 Choice of the t_m parameter

The t_m parameter is the end time of the analysis. The nominal choice for the End-game data set is $t_m = 300 \mu s$. This value is optimized performing a t_m scan (see Sec. 7.3). As explained in [1] Sec. 7.3 and in [2] Sec. 4.3, there is a trade off increasing the length of the fast rotation signal between improving the frequency resolution and adding exponentially growing statistical noise at late time. The t_m scan allows to optimized this trade off. The exact value of t_m is optimized in the same fashion as t_s in order to match the fast rotation signal intensity with 1.

4.3 Choice of the t_0 parameter

The t_0 parameter corresponds to the time when the centroid of the longitudinal profile of the beam is detected by calorimeter #1 right after injection (first turn of the beam into the ring). Given the saturation and the beam-line positron contamination, the data corresponding to the first turn is not recorded. The t_0 value therefore needs to be optimized. The iterative optimization procedure is explained in [1] Sec. 6. It relies on a χ^2 minimization fitting for the background of the cosine Fourier transform of the fast rotation signal. Figure 5 shows the results of the four iterations: the optimum background fit for each iteration and the χ^2 distribution of the background fit as a function of t_0 . After the fourth iterations, the optimized t_0 value is 129.504 ns. This value is consistent with the work presented in [7]. Figure 6 shows the optimum background fit after the t_0 optimization procedure.

4.4 Frequency distribution

Once the t_0 optimization is performed, the optimum cosine Fourier transform is available. It can be corrected for its background using the background fit. The correction corresponds to subtracting the background fit to the cosine Fourier transform. Figure 7 shows the cosine Fourier transform and its corrected version limited to the collimator aperture. Figure 8 shows the zoomed-out version for the full frequency range of 150 kHz used for the analysis. The measured average and width of the cyclotron frequency distribution are respectively 6,698.65 kHz and 8.37 kHz.

4.5 Radial distribution

The frequency distribution can be converted to the radial distribution as explained in [1] Sec. 8. Figure 9 shows the radial distribution in the beam coordinate (the so-called “magic radius” of 7112 mm corresponds to $r=0$, positive (negative) r values correspond to radially outward (inward) positions) limited to the collimator aperture (± 45 mm). Figure 10 shows the same distribution in the ring coordinate limited and not limited to the collimator aperture.

The equilibrium radius (average of the radial distribution) is 6.35 mm and the width of the distribution is 9.19 mm.

4.6 Electric field correction estimation

The electric field correction is estimated from eq. (1), given the radial distribution in Fig. 9, to be $C_E = -467$ ppb. The field index in eq. (1) is expressed (for the continuous quad approximation) as:

$$n = 1 - \nu_x^2, \quad (5)$$

where ν_x is the radial tune expressed as:

$$\nu_x = 1 - f_{cbo}/f_c, \quad (6)$$

where $f_{cbo} = 366.98$ kHz is the CBO frequency extracted from the 9-parameter wiggle fit and $f_c = 6,698.65$ kHz is the average cyclotron frequency. The resulting field index used to estimate the electric field correction is $n = 0.1066$. This value is in good agreement with the field index measurement done by the tracker and calorimeter teams.

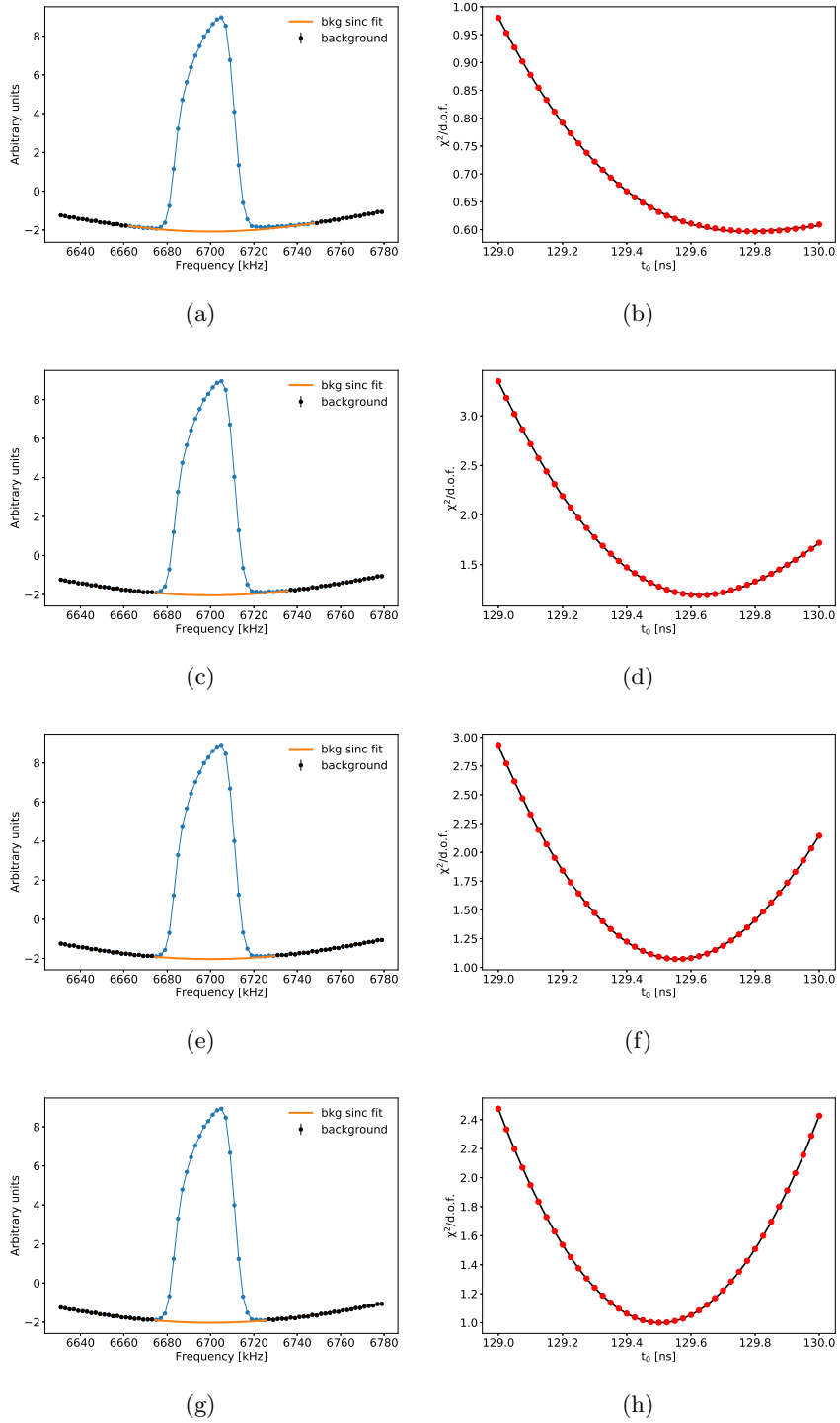


Figure 5: Results of the four iterations (from top to bottom) of the t_0 optimization procedure. The figures on the left show the cosine Fourier transform with its cardinal sine background fit for the optimum t_0 value. The figures on the right show the χ^2 distribution of the background fit as a function of t_0 . The optimized t_0 value after four iterations is 129.504 ns.

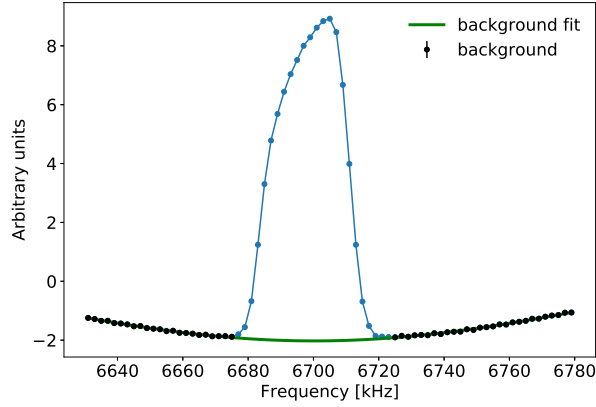


Figure 6: Optimum cardinal sine background fit to the cosine Frequency distribution.

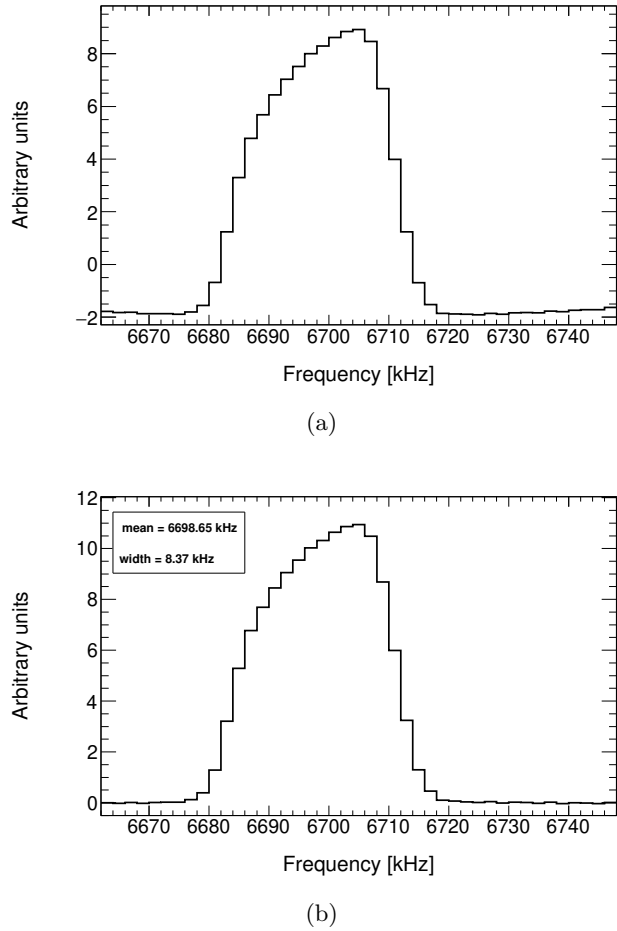


Figure 7: Frequency distributions: (a) cosine Fourier transform, and (b) corrected cosine Fourier transform limited to the collimator aperture.

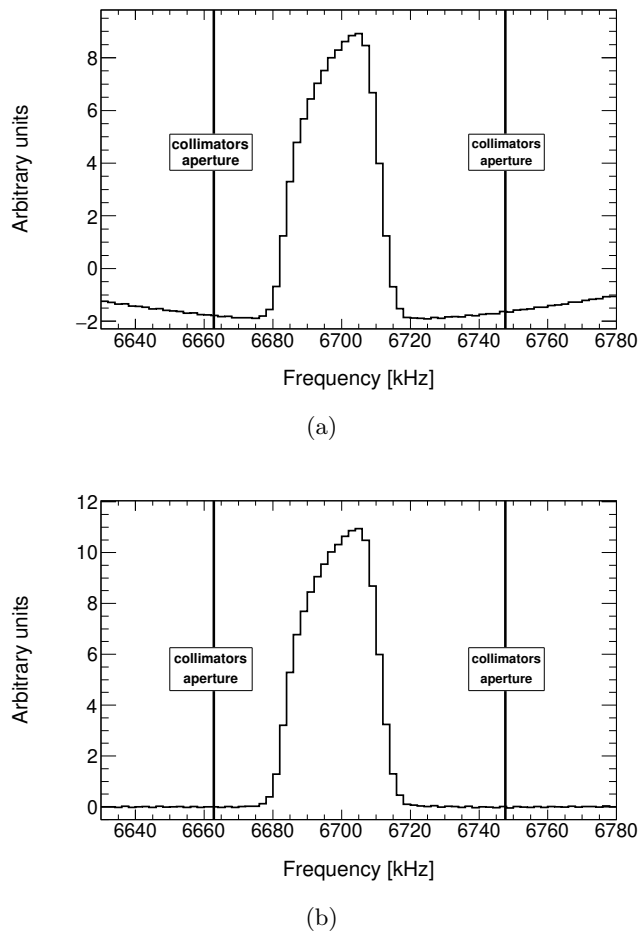


Figure 8: Frequency distributions: (a) cosine Fourier transform, and (b) corrected cosine Fourier transform for the full frequency range used in the analysis.

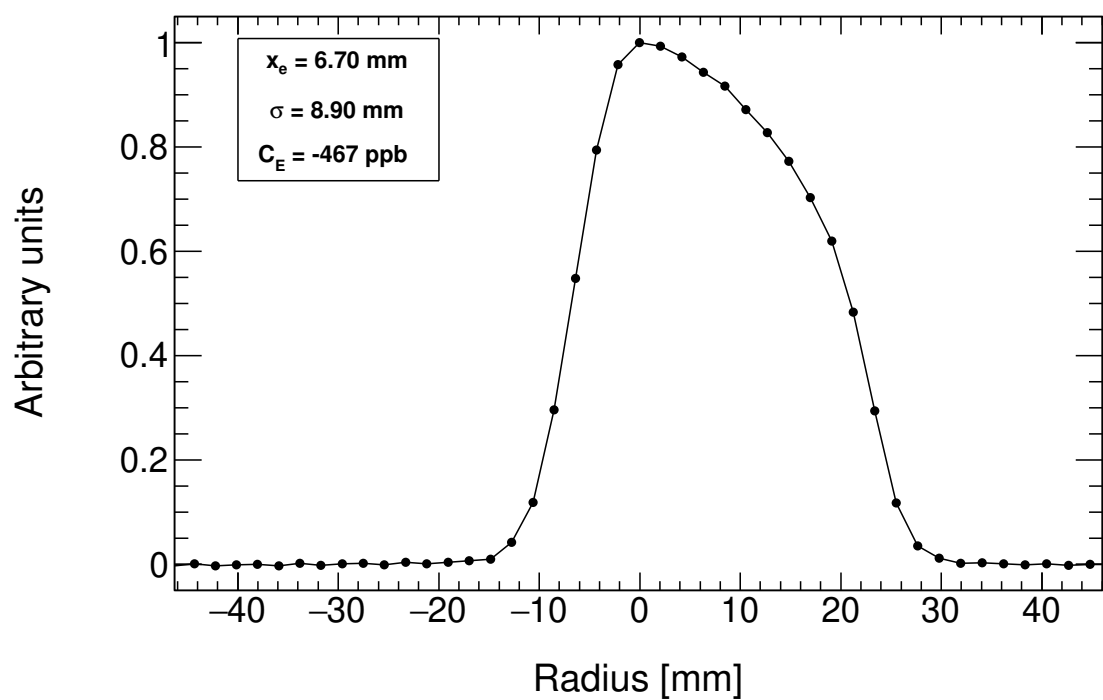
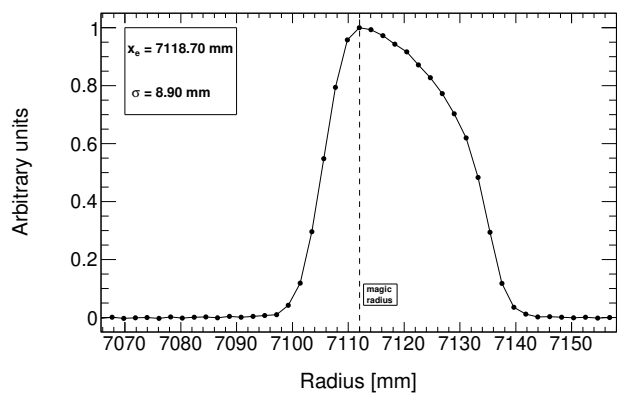
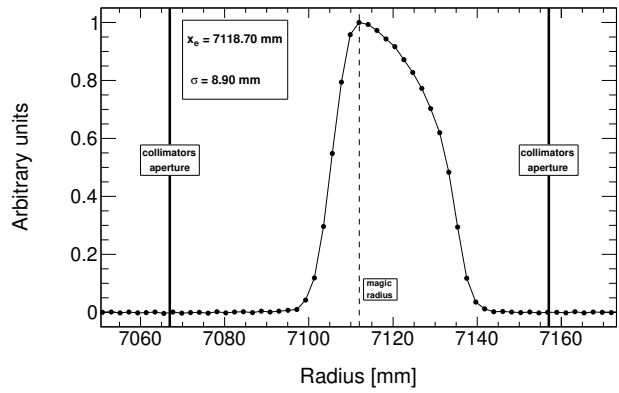


Figure 9: Radial distribution in the beam coordinate limited to the collimator aperture.



(a)



(b)

Figure 10: Radial distribution in the ring coordinate: (a) limited to the collimator aperture, and (b) not limited to the collimator aperture but to the full range of the analysis.

5 Per-calorimeter and per-bunch analysis

This section will detail the fast rotation analysis performed per-calorimeter and per-bunch.

5.1 Per-calorimeter analysis

The results presented in Sec. 4 correspond to all the 24 calorimeters combined, i.e., the results correspond to the azimuthal averaging around the ring. It is important to perform the analysis per-calorimeter to ensure the results are consistent all around the ring. Any significant difference would have to be understood and, if needed, included in the anomalous spin precession analysis. The per-calorimeter fast rotation analysis is almost identical to the one performed on all the calorimeters combined. The only difference being that the definition of the background is fixed to the ones from the nominal analysis. Not fixing the background definition would introduce a systematic bias in the per-calorimeter results, thus making less straightforward the comparisons of the results. The t_0 parameter is optimized for each calorimeter and is expected to jump by a 24th of the cyclotron revolution period between two consecutive calorimeters. Figure 11 shows the optimized t_0 values as a function of calorimeter number. The statistical uncertainty on each data point (see Sec. 6.3) is about 0.029 ns and thus too small to be seen. The fit to the data point returns:

$$t_0 = 6.219(1) \pm 123.28(1) \text{ ns.} \quad (7)$$

The number in () is the uncertainty associated with the last digit, i.e., 6.219(1) means 6.219 ± 0.001 and 123.28(1) means 123.28 ± 0.01 . The magic cyclotron period of 149.14 ns corresponds to a time shift of 6.214 ns between two consecutive calorimeters. From the nominal measured cyclotron frequency of 6,698.65 kHz, using all the calorimeters and bunches, the measured cyclotron period is 149.28 and thus the time shift is 6.220 ns. The time shift obtained from the per-calorimeter results is statistically 1 standard deviation away from the expected results of 6.220 ns.

Figure 12 shows the radial distributions for all the 24 calorimeters overlaid. The by-eye agreement is satisfying. Fig. 13 shows x_e , σ and C_E as a function of calorimeter number. The error bars are the statistical uncertainty. The results per-calorimeter are statistically in reasonable agreement, the largest deviation being of the order of 4 standard deviations¹. Assuming that each calorimeter has the same statistical uncertainty, the averaging of them all yields:

¹The systematic uncertainty is expected to be larger than the statistical uncertainty but is not estimated per-calorimeter.

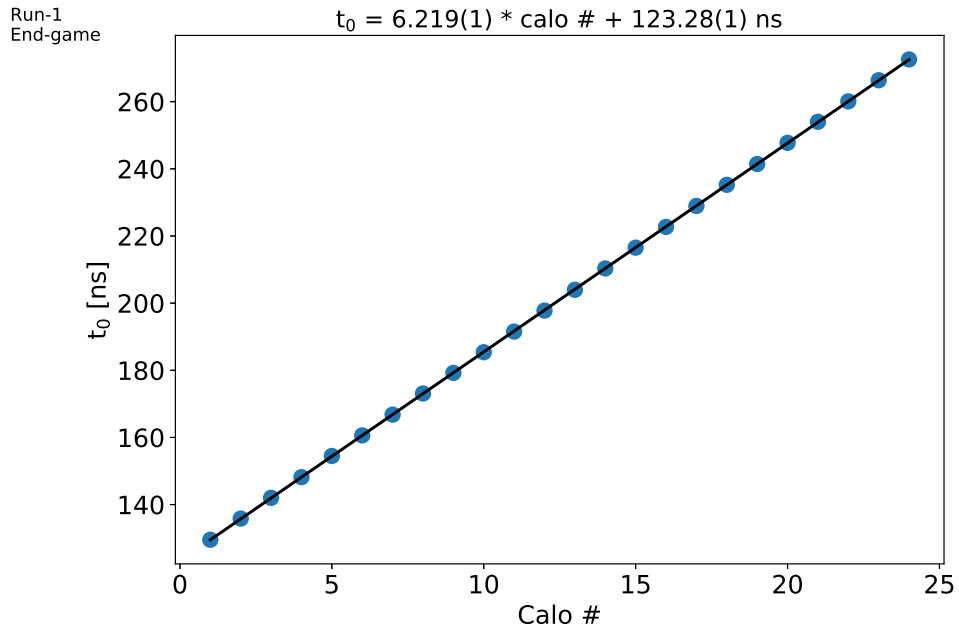


Figure 11: Optimized t_0 value as a function of calorimeter number. The black line is a linear fit to the data point. The fit results gives the t_0 variation as a function of calorimeter number: $t_0 = 6.219(1) \cdot \text{Calo } \# + 123.28(1) \text{ ns}$.

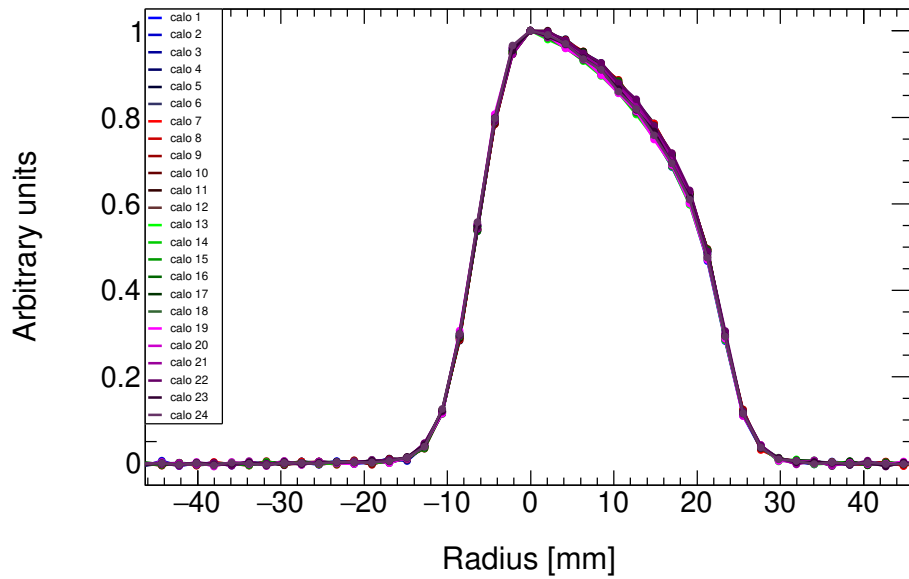


Figure 12: Radial distributions for all the 24 calorimeters overlaid.

$$\begin{aligned}x_e &= 6.72 \text{ mm}, \\ \sigma &= 8.88 \text{ mm}, \\ C_E &= -466 \text{ ppb},\end{aligned}$$

which are in good agreement with the results presented previously for all the calorimeters combined. The standard errors² of the per-calorimeter results are:

$$\begin{aligned}\delta x_e &= 0.015 \text{ mm}, \\ \delta \sigma &= 0.006 \text{ mm}, \\ \delta C_E &= 0.64 \text{ ppb},\end{aligned}$$

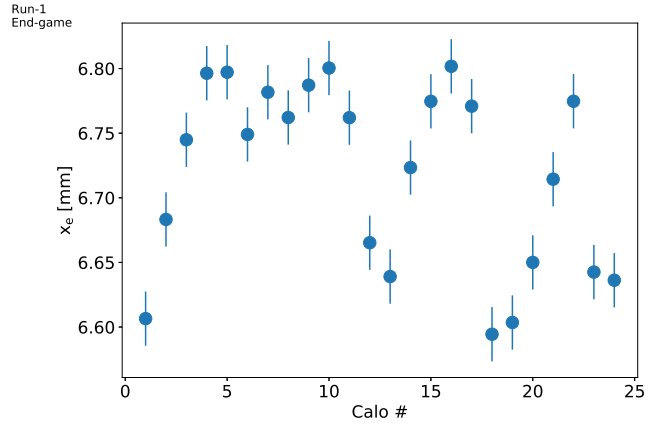
which for x_e and C_E are respectively three and two times the statistical uncertainty estimated when performing the analysis on all the calorimeters combined. This indicates some non-statistical effect in the per-calorimeter analysis³. Table 1 summarizes all the numbers.

²The standard error is the uncertainty on the average value using the spread of the results.

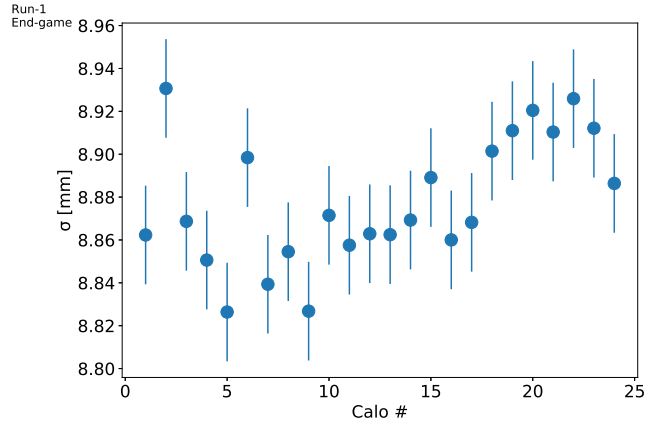
³In the presence of statistical effect only: the results and the associated uncertainties should be the same if performing the analysis on the combined inputs or combining the outputs of the individual analysis.

	t_0 [ns]	x_e [mm]	σ [mm]	C_E [ppb]
calo #1	129.527	6.607	8.862	-459.6
calo #2	135.825	6.683	8.931	-468.0
calo #3	142.009	6.745	8.869	-467.0
calo #4	148.157	6.796	8.851	-468.4
calo #5	154.476	6.797	8.826	-466.8
calo #6	160.603	6.749	8.898	-469.2
calo #7	166.792	6.782	8.839	-466.9
calo #8	173.078	6.762	8.855	-466.9
calo #9	179.228	6.787	8.827	-466.3
calo #10	185.378	6.800	8.871	-470.0
calo #11	191.532	6.761	8.858	-467.1
calo #12	197.787	6.665	8.863	-462.6
calo #13	203.981	6.639	8.862	-461.2
calo #14	210.329	6.723	8.867	-465.9
calo #15	216.523	6.775	8.889	-469.8
calo #16	222.714	6.802	8.860	-469.3
calo #17	228.947	6.771	8.868	-468.3
calo #18	235.245	6.594	8.901	-461.6
calo #19	241.438	6.604	8.911	-462.7
calo #20	247.749	6.650	8.920	-465.6
calo #21	254.015	6.714	8.910	-468.2
calo #22	260.099	6.775	8.926	-472.3
calo #23	266.391	6.643	8.912	-464.7
calo #24	272.587	6.636	8.886	-462.7

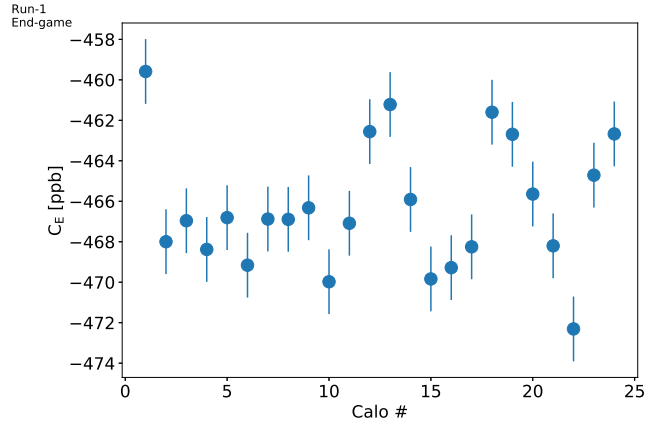
Table 1: Per-calorimeter results of the fast rotation analysis.



(a)



(b)



(c)

Figure 13: Analysis results of the fast rotation analysis per-calorimeter: (a) x_e , (b) σ , and (c) C_E . The error bars show the statistical uncertainty (see Sec. 6.3).

5.2 Per-bunch analysis

Figure 39 in App. A shows that the 8 bunches in the accelerator cycle have different longitudinal profiles. Given the length of the incoming pulse of about 200 ns and the time inhomogenous kick provided by the three kickers inside the ring, one can expect different stored radial distributions for each bunch. It is therefore interesting to look at the fast rotation results for each bunch individually⁴ combining all the calorimeters together. Similarly to the per-calorimeter analysis, the definition of the background is fixed to the ones from the nominal analysis. Not fixing the background definition would introduce a systematic bias in the per-bunch results, thus making less straightforward the comparisons of the results. The t_0 parameter is optimized for each bunch and is expected to be randomly distributed because of the differences in the beam profiles (the time centroid of each bunch depends on its profile). Figure 15(a) shows the optimized t_0 values as a function of bunch number. The statistical uncertainty on each data point (see Sec. 6.2) is about 0.02 ns and thus too small to be seen. Assuming each bunch has the same statistical uncertainty, the averaging of the t_0 values yields:

$$t_0 = 129.217 \text{ ns},$$

which is close to the optimized t_0 value when all the calorimeters and bunches are combined together: $t_0 = 127.504$ ns. Figure 14 shows the radial distributions for all the 8 bunches overlaid.

Fig. 15(b, c, d) show x_e , σ , and C_E as a function of bunch number. The error bars are the statistical uncertainty. Assuming that each bunch has the same statistical uncertainty, the averaging of them all yields:

$$\begin{aligned} x_e &= 6.70 \text{ mm}, \\ \sigma &= 8.88 \text{ mm}, \\ C_E &= -466 \text{ ppb}, \end{aligned}$$

which are in good agreement with the results presented previously for all the calorimeters and bunches combined. These results indicate that the per-bunch and per-calorimeter information can be linearly combined together before or after performing the fast rotation analysis. Table 2 summarizes all the numbers.

⁴The anomalous spin precession frequency is nominally performed combining all the bunches together.

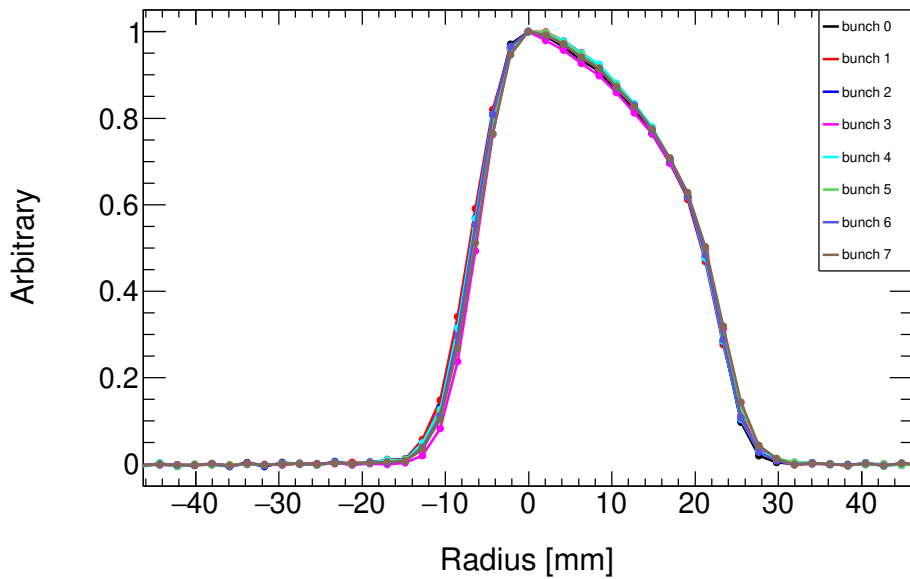


Figure 14: Radial distributions for all the 8 bunches overlaid.

	t_0 [ns]	x_e [mm]	σ [mm]	C_E [ppb]
bunch #0	126.924	6.610	8.816	-456.7
bunch #1	129.585	6.454	8.947	-457.7
bunch #2	126.098	6.552	8.894	-459.0
bunch #3	136.479	7.009	8.803	-476.3
bunch #4	127.228	6.589	8.910	-461.9
bunch #5	134.259	6.756	8.923	-471.2
bunch #6	116.601	6.669	8.849	-461.8
bunch #7	136.564	6.973	8.934	-483.1

Table 2: Per-bunch results of the fast rotation analysis.

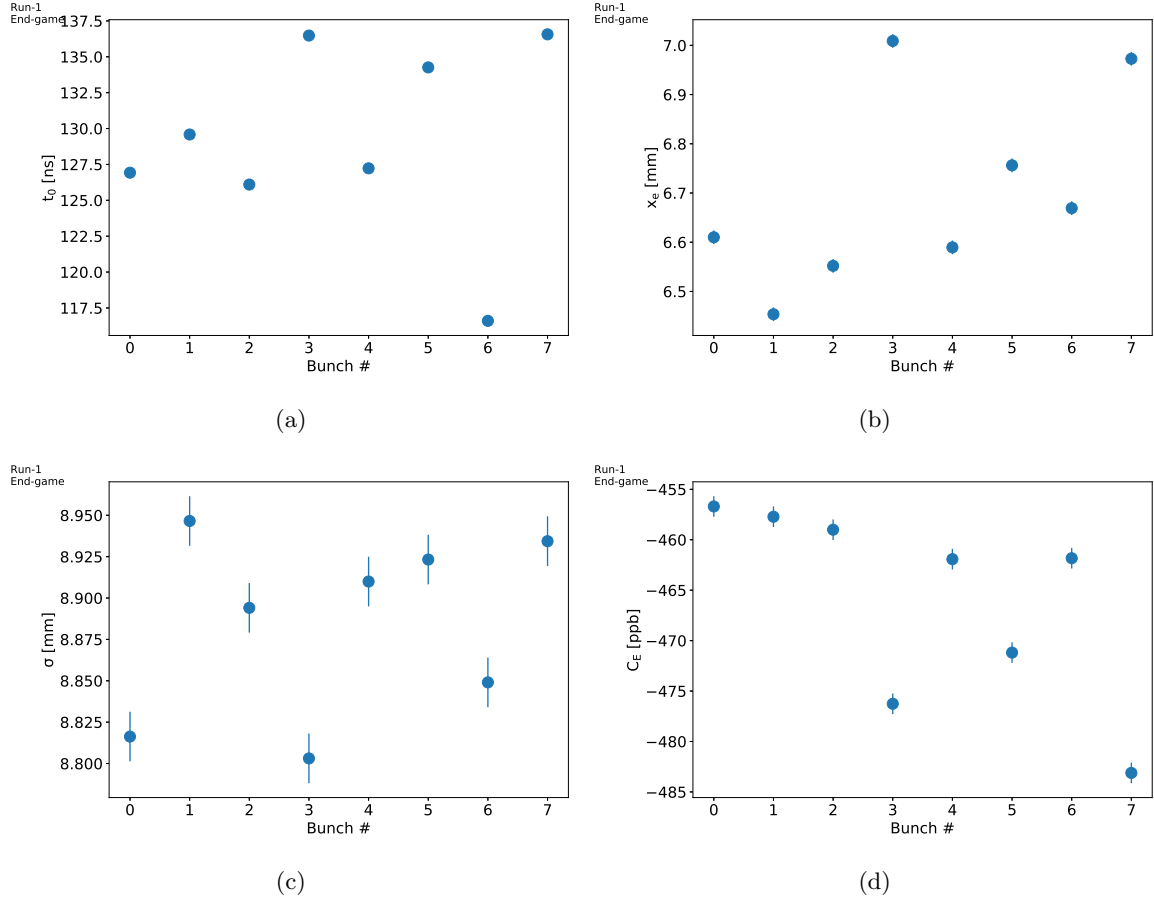


Figure 15: Analysis results of the fast rotation analysis per-bunch: (a) t_0 (b) x_e , (c) σ , and (d) C_E . The error bars show the statistical uncertainty (see Sec. 6.2).

	t_0 [ns]	x_e [mm]	σ [mm]	C_E [ppb]
nominal	0.006	0.005	0.005	0.34
per-bunch	0.019	0.014	0.015	1.02
per-calorimeter	0.029	0.021	0.023	1.60

Table 3: Statistical uncertainty on the results of the nominal, per-bunch and per-calorimeter fast rotation analysis.

6 Statistical uncertainty

6.1 Nominal analysis

This section will detail the estimation of the statistical uncertainty. The estimation relies on bootstrapping to generate many pseudo data set with varied statistics. Figure 16 shows a diagram of the procedure. Each pseudo data set is generated from varying the statistics of the original positron counts histogram of all the 24 calorimeters combined. The number of entries N_i in each bin i is varied randomly by either $+$ or $- \sqrt{N_i}$, i.e., the variation follows a Poisson statistics (the positron counts histogram corresponds to a counting experiment). The fast rotation analysis is performed on each of the many pseudo data in order to get an ensemble of results from which is estimated the statistical uncertainty. The definition of the background, i.e. which data point are defined as background, is fixed for analyzing all the pseudo data set. This is necessary to avoid a systematic effect due to the background definition⁵. The parameters t_0 , t_s and t_m are optimized for each pseudo data set. Figure 17 shows the ensemble of results for the nominal fast rotation analysis. The statistical uncertainty is taken as the standard deviation of the distribution of results. Table 3 summarizes the numbers. The statistical uncertainty appears to be very small and will be negligible in comparison to the systematic uncertainties (see Sec. 7). Figure 18 shows the statistical correlation distributions between the results. It appears that x_e is very strongly anti-correlated with t_0 . This is explained by the fact that changing t_0 skews the cosine Fourier transform to the right or to the left, therefore shifting its average value one way or the other.

6.2 Per-bunch analysis

The procedure above is used to estimate the statistical uncertainty of the results per-bunch with the 24 calorimeter combined, i.e., the statistics is an 8th of the nominal statistics.. The estimation is performed using bunch #0. It is assumed that the statistical uncertainty of the other 7 bunches is the same. Figure 19 shows the distributions of the results. The statistical

⁵This effect would translate into multiple peaks in the distribution of the results. These peaks would have the same standard deviation but different average values.

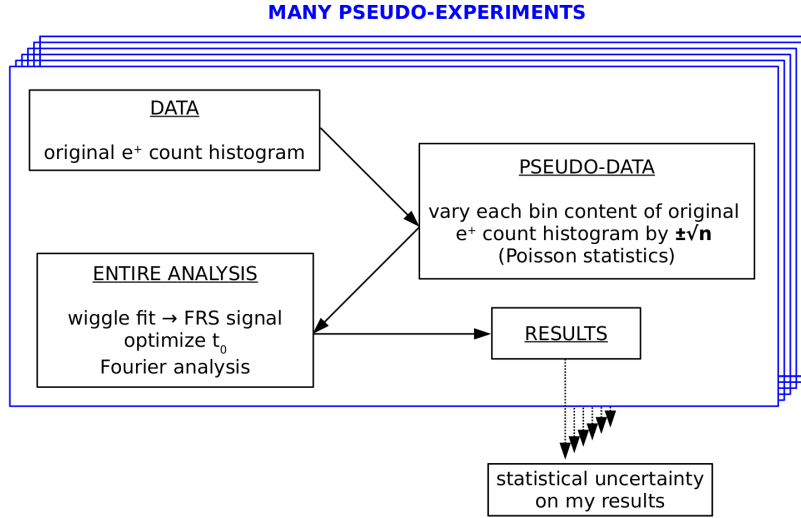


Figure 16: Diagram of the procedure for estimating the statistical uncertainty on the fast rotation results.

uncertainty scales as expected: $\sqrt{8}$ times bigger than the values for the nominal analysis which accounts for analyzing 1 bunch versus analyzing 8 combined.

6.3 Per-calorimeter analysis

The procedure above is used to estimate the statistical uncertainty of the results per-calorimeter with the 8 bunches combined, i.e., the statistics is a 24th of the nominal statistics. The estimation is performed using calorimeter #1. It is assumed that the statistical uncertainty of the other 23 calorimeters is the same. Figure 20 shows the distributions of the results. The statistical uncertainty scales as expected: $\sqrt{24}$ times bigger than the values for the nominal analysis which accounts for analyzing 1 calorimeter versus analyzing 24 combined.

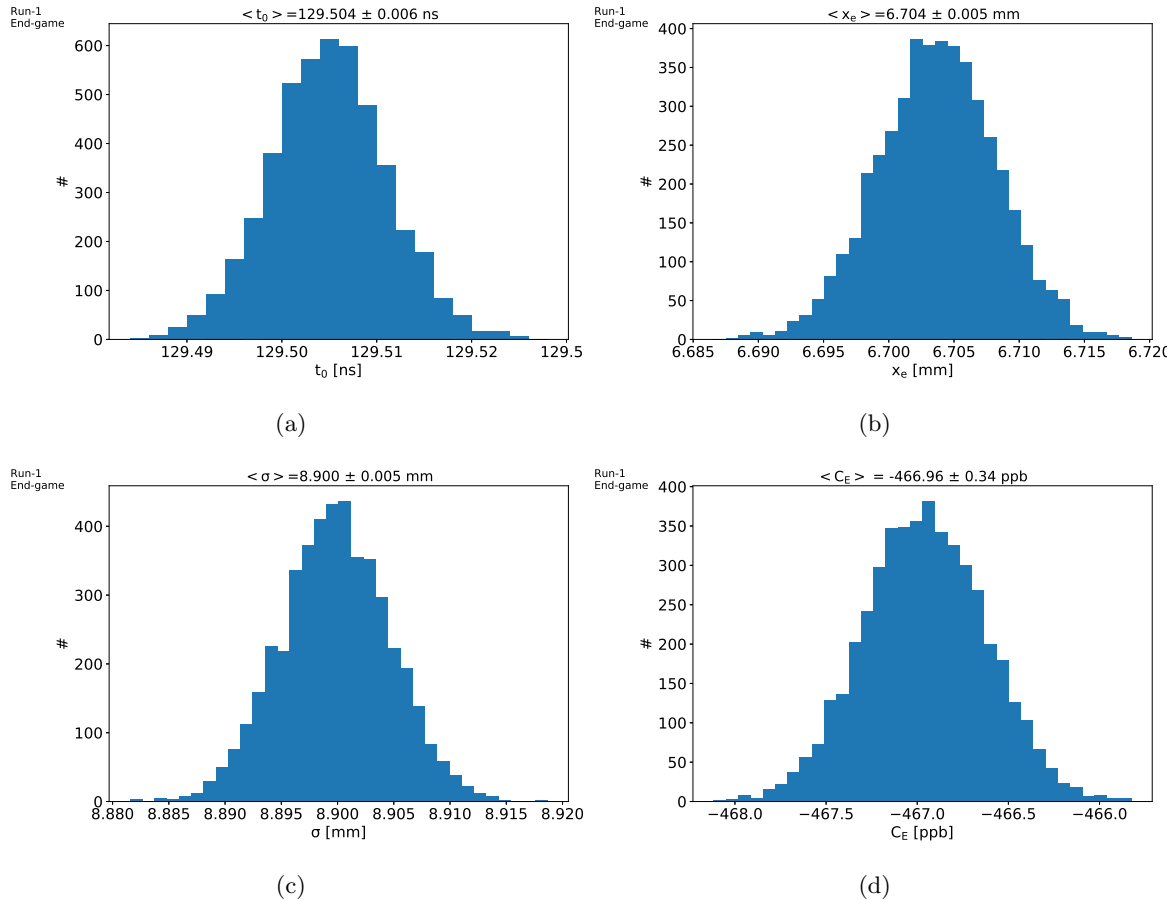


Figure 17: Analysis results of the pseudo data for the nominal analysis: (a) optimized t_0 , (b) x_e , (c) σ , and (d) C_E . The title of each histogram corresponds to the mean and standard deviation of the distribution.

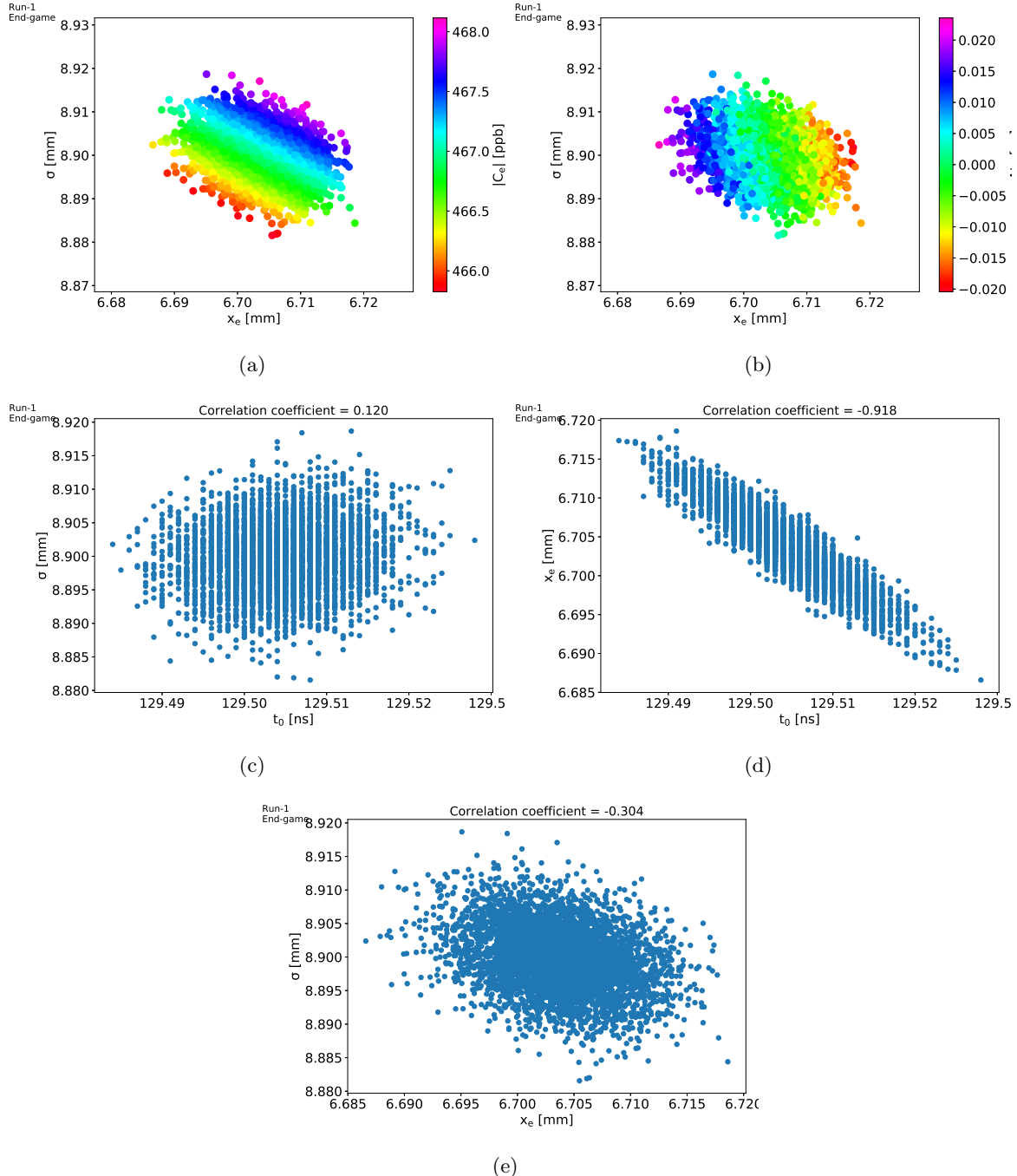


Figure 18: Statistical correlation between: (a) C_E , σ and x_e , (b) $\Delta t_0 = \langle t_0 \rangle - t_0$, σ and x_e , (c) σ and t_0 , (d) x_e and t_0 , and (e) σ and x_e , The title of the 2D histograms corresponds to the correlation coefficient between the two variables.

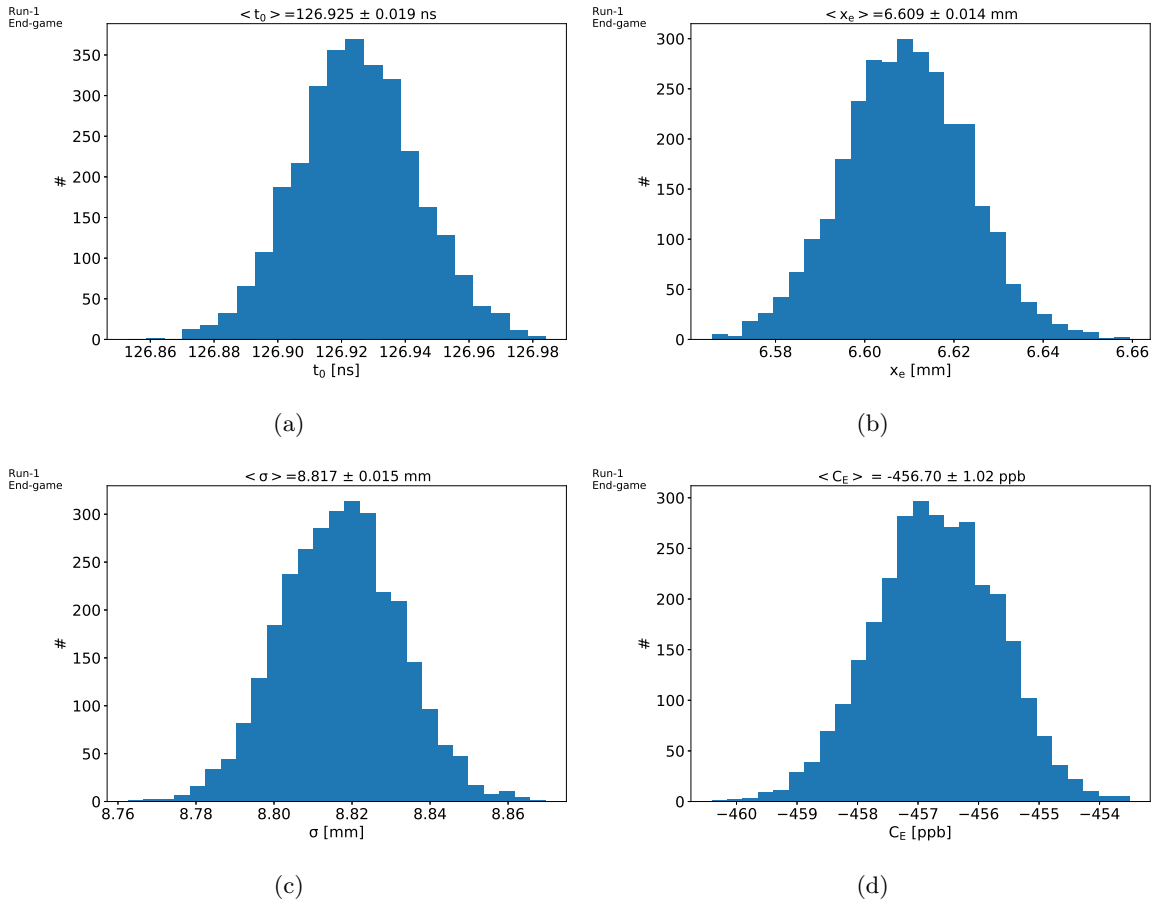


Figure 19: Analysis results of the pseudo data for bunch #0: (a) optimized t_0 , (b) x_e , (c) σ , and (d) C_E . The title of each histogram corresponds to the mean and standard deviation of the distribution.

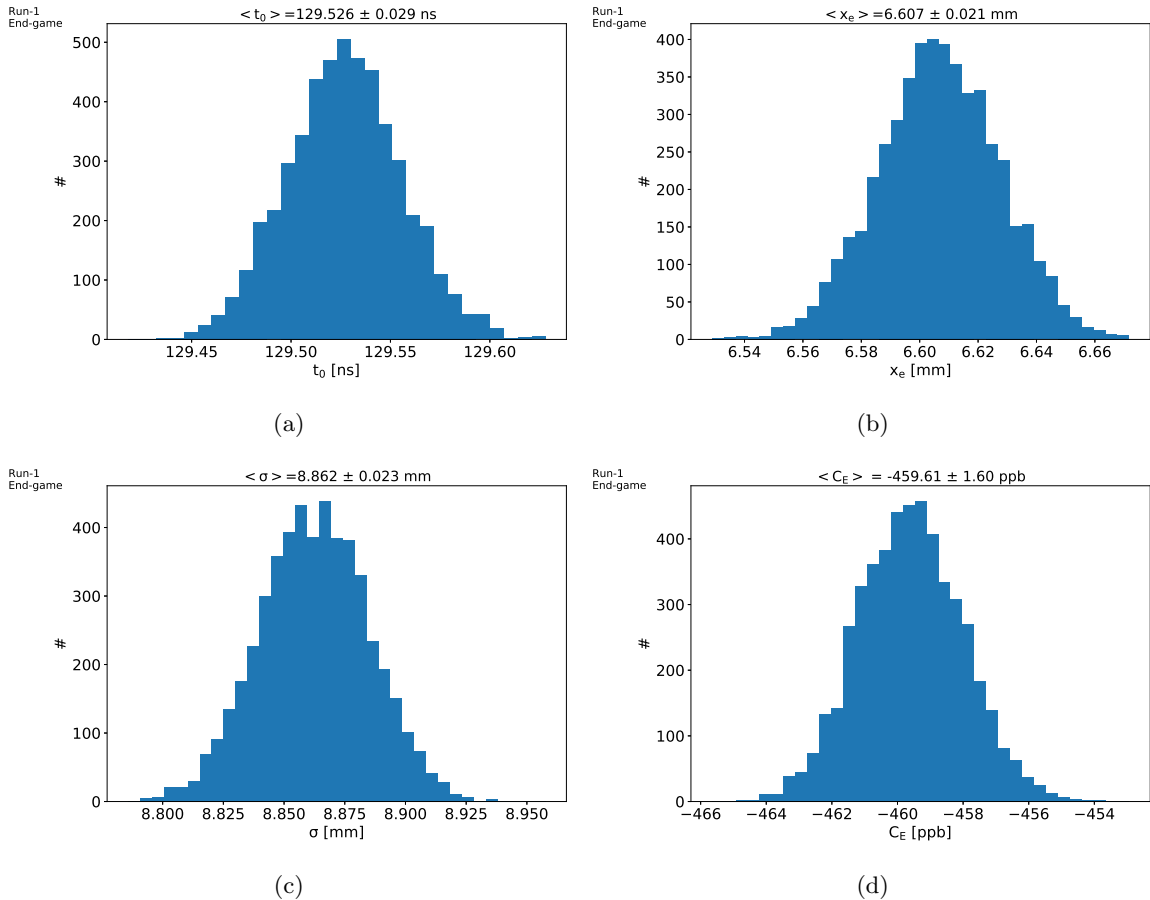


Figure 20: Analysis results of the pseudo data for calorimeter #1: (a) optimized t_0 , (b) x_e , (c) σ and (d) C_E . The title of each histogram corresponds to the mean and standard deviation of the distribution.

	t_0 [ns]	x_e [mm]	σ [mm]	C_E [ppb]
cardinal sine	129.504	6.70	8.90	-467
error function	129.504	6.70	8.90	-467
triangle function	129.532	6.68	8.90	-466
systematic	0.02	0.01	0.01	1

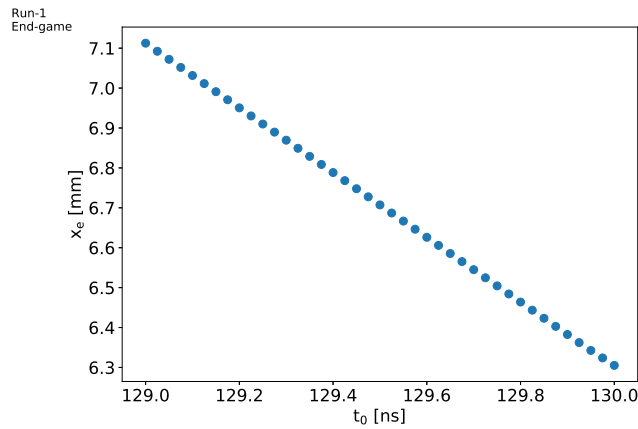
Table 4: Estimation of the t_0 systematic uncertainty. The systematic uncertainty is estimated as half the maximum variation between the results from the three background fit functions.

7 Systematic uncertainties

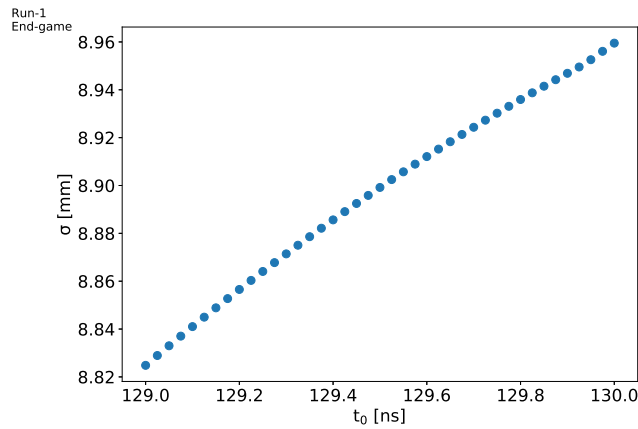
The philosophy of the systematic uncertainties estimation is to vary or turn on/off the various analysis parameters and take the value of the uncertainties as half the maximum variation in the results in order to obtain a symmetric \pm uncertainty.

7.1 t_0 systematic

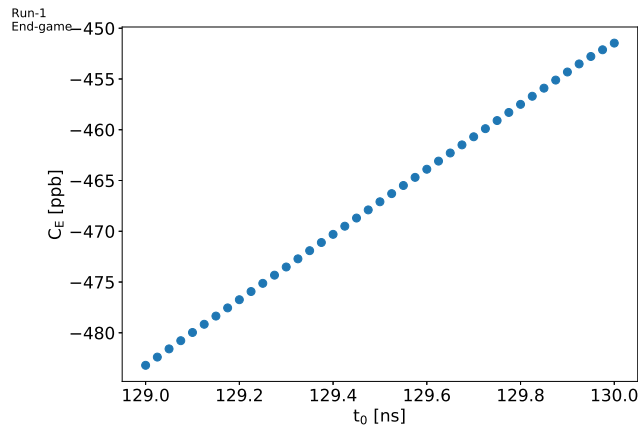
As shown in [2] Sec. 4.1, the sub-ns knowledge of the t_0 parameter is essential in order to reach the dozens of ppb uncertainty on C_E . Figure 21 shows how x_e , σ and C_E vary as a function of t_0 . The small change in σ drives the limited change of 35 ppb in C_E . The large relative variation of x_e does not significantly impact C_E given that x_e and σ contribute with the same weight to the C_E calculation and $\sigma = 8.9 > x_e = -6.7$ mm. The source of uncertainty from t_0 , as detailed in [2] Sec. 4.1, is estimated by performing its optimization, and then the remaining analysis, using three different fit functions for the background: cardinal sine, error function, triangle-based function. Table 4 shows the analysis results using the three functions. The systematic uncertainty is estimated as half the maximum difference in the results from the three background fit functions.



(a)



(b)



(c)

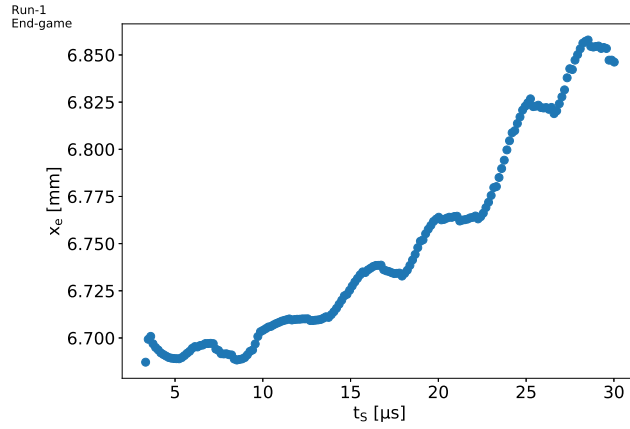
Figure 21: Results of the fast rotation analysis as a function of t_0 for a 1 ns range: (a) x_e , (b) σ , and (c) C_E .

7.2 t_s systematic

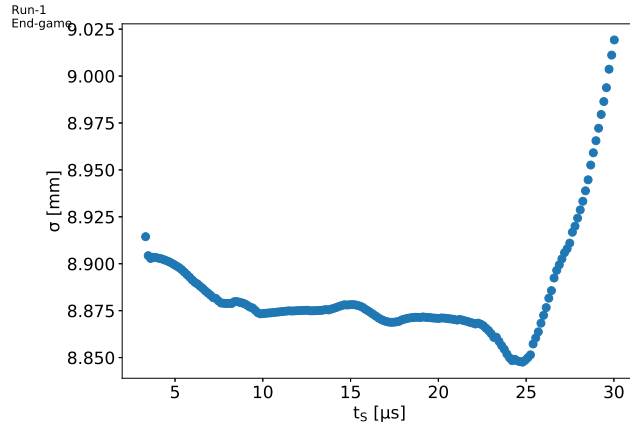
In an ideal world, the fast rotation Fourier analysis would be performed from $t_s = t_0$ in order to avoid the complication due to missing early data (see Sec. 4.1). The ideal world would also allow to start the analysis at $t_s = 30 \mu s$, time at which the anomalous spin precession frequency analysis starts. The main reason for skipping the first $30 \mu s$ is to leave time for the beam to stabilize after the scraping period ends at about $25 \mu s$ (the first-to-second step scraping transition happens at $7 \mu s$). Scraping shifts the closed orbit of the beam both vertically and horizontally. Therefore using data before $25 \mu s$ might bias the reconstructed radial distribution that would end up not being fully representative of the distribution of the stored beam after $25 \mu s$. There are also other effects that are more important early time in the fill versus later in the fill: instantaneous pile-up rate, gain correction, muon loss. It is thus essential to show that the fast rotation results change within an acceptable range between the earliest possible t_s and $t_s = 30 \mu s$.

The t_s scan (see [2] Sec. 4.2) is performed using the triangle-based background fit function. The t_0 value is fixed for all the t_s values to the one optimized for the nominal analysis ($t_s = 4 \mu s$) given the earliest the start time the more the t_0 optimization performs well. The definition of the background is fixed to the one defined by the nominal analysis. Figure 22 shows the results of the analysis as a function of t_s between 3 and $30 \mu s$. Figure 23 shows the same results only up to $25 \mu s$. The statistical uncertainty on each point is not shown but is increasing exponentially with time since the fast rotation statistics decreases exponentially (muon life-time). Figure 24 shows the background fit using the triangle-based function for six different t_s values. Figure 25 shows the information related to the background fit quality: $\chi^2/\text{d.o.f.}$ and residuals.

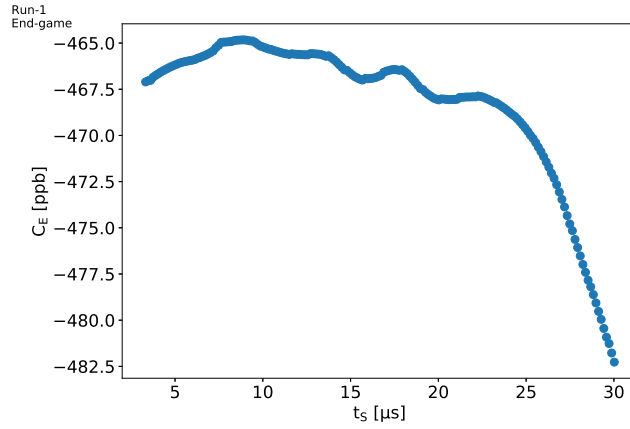
The trend of the results cannot currently be explained with satisfaction. Tentative explanations could be made using arguments related to beam dynamics and scraping. For instance, the first step scraping moves the radial closed orbit at early time and scrapes the radial tail of the beam, thus shifts the equilibrium radius and shrinks the width of the beam. The second step then re-centers the beam and allows its width to grow and its equilibrium radius to move. These kind of by-hand arguments need to be thoroughly investigated with full scale high statistics simulations using **BMAD** and **GM2RINGSIM**. For now, and for the scope of estimating a systematic uncertainty, half the maximum variation in the results for the t_s scan from 3 to $25 \mu s$ is used as the systematic uncertainty and is under control for the Run-1. The upper limit of $25 \mu s$ is motivated by studies done with toy Monte Carlo simulations [2] and might be sufficient since scraping is over by that time. The last $5 \mu s$, between 25 and $30 \mu s$, to reach the analysis start time of the anomalous spin precession frequency remain for now un-accounted for.



(a)

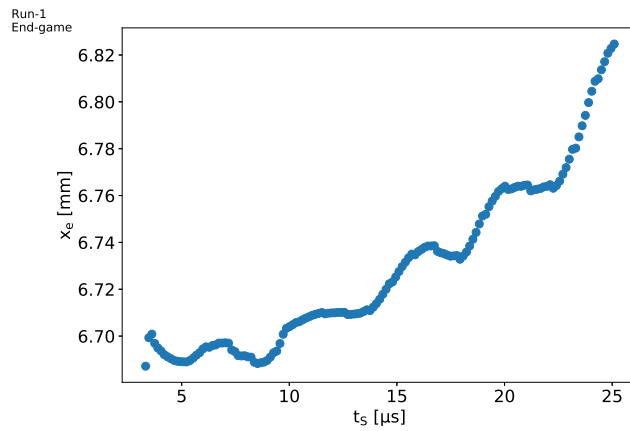


(b)

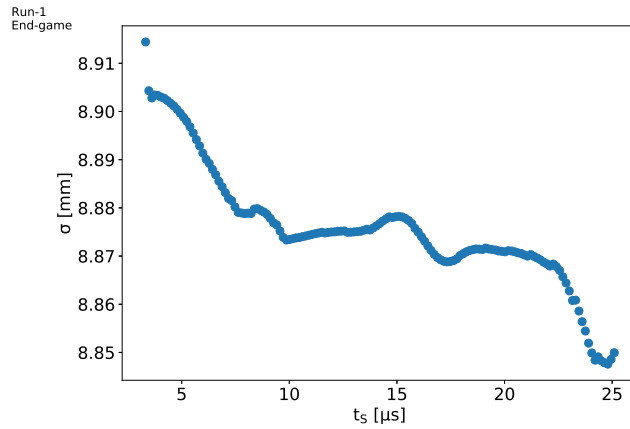


(c)

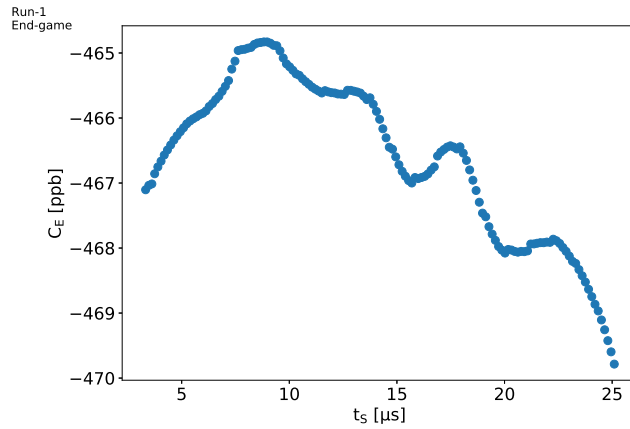
Figure 22: Results of the fast rotation analysis as a function of t_s for a 30 μ s range using the triangle-based background fit function: (a) x_e , (b) σ , and (c) C_E .



(a)



(b)



(c)

Figure 23: Results of the fast rotation analysis as a function of t_s for a 25 μs range using the triangle-based background fit function: (a) x_e , (b) σ , and (c) C_E .

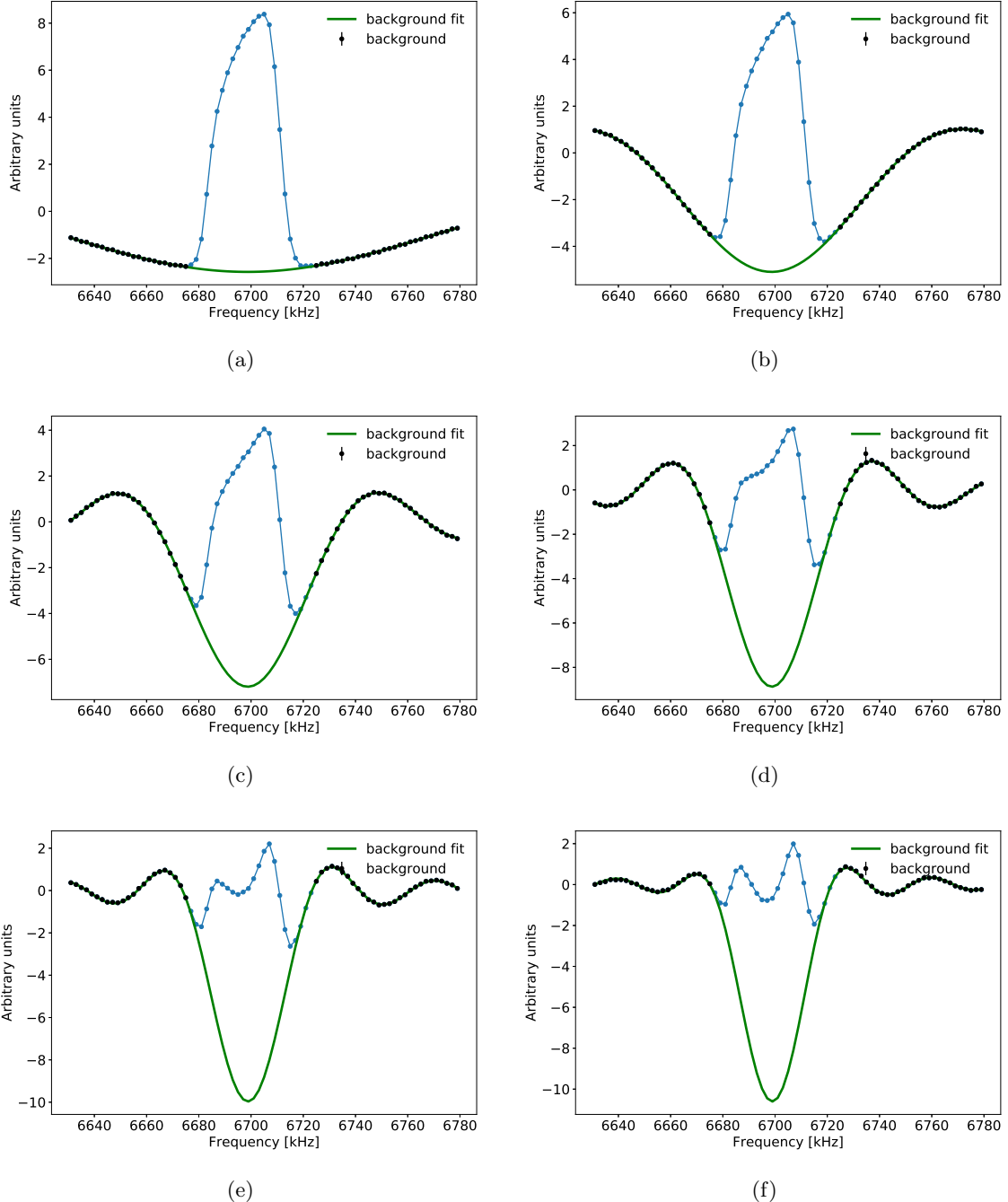
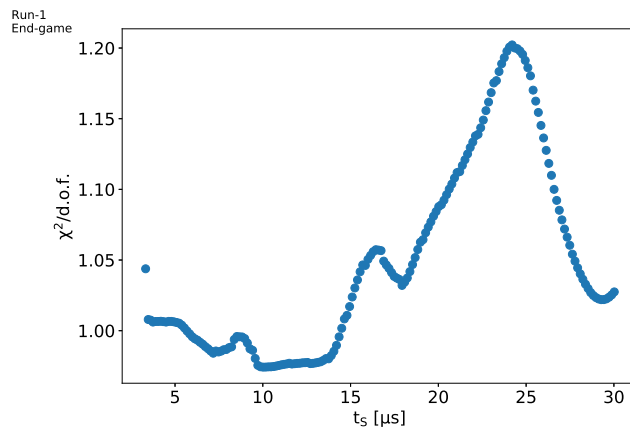
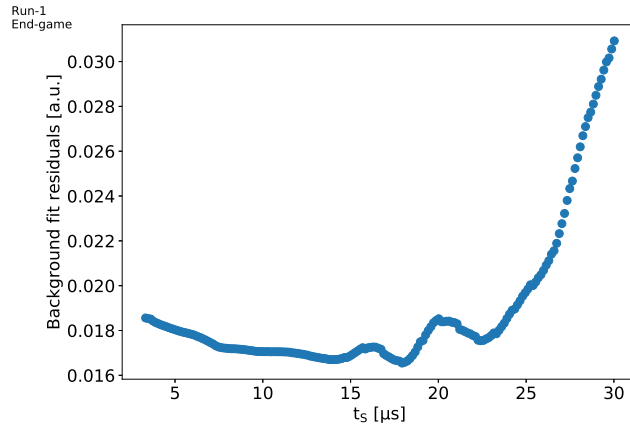


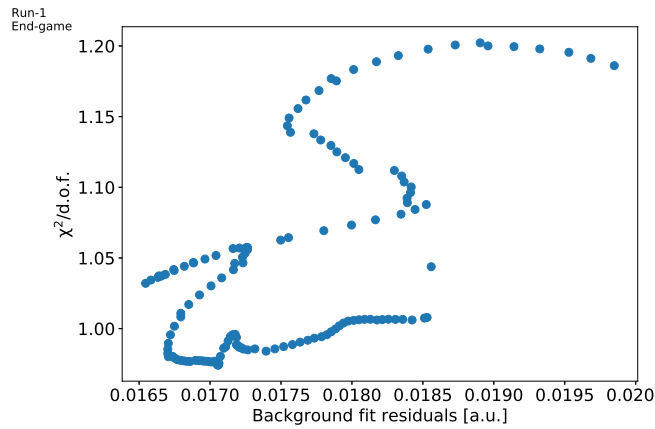
Figure 24: Background fit of the cosine Fourier transform using the triangle-based function:
(a) $t_s = 5 \mu\text{s}$, (b) $t_s = 10 \mu\text{s}$, (c) $t_s = 15 \mu\text{s}$, (d) $t_s = 20 \mu\text{s}$, (e) $t_s = 25 \mu\text{s}$, (f) $t_s = 30 \mu\text{s}$.



(a)



(b)

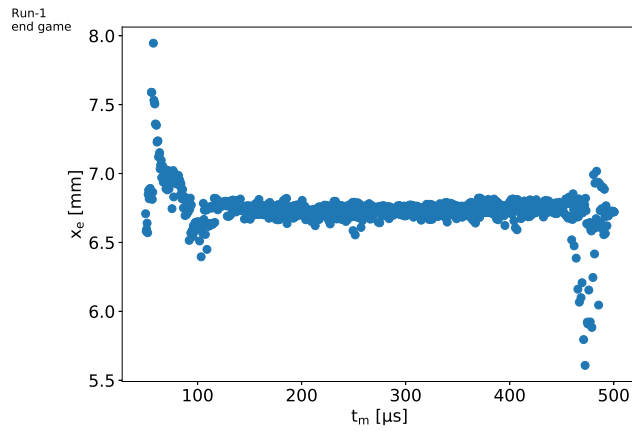


(c)

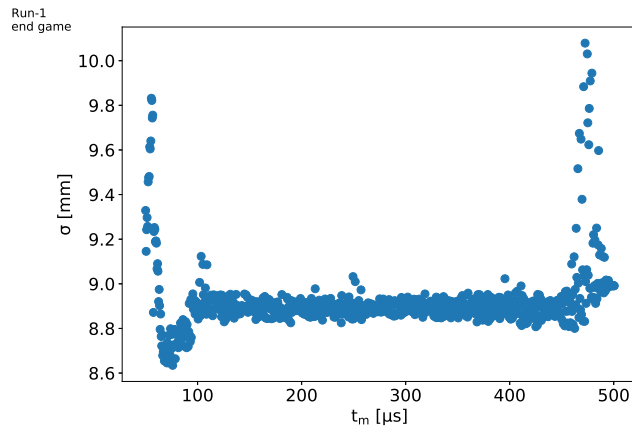
Figure 25: Background fit information for the triangle-based function: (a) $\chi^2/\text{d.o.f.}$ as a function of t_s , (b) fit residuals as a function of t_s , and (c) $\chi^2/\text{d.o.f.}$ as a function of fit residuals.

7.3 t_m systematic

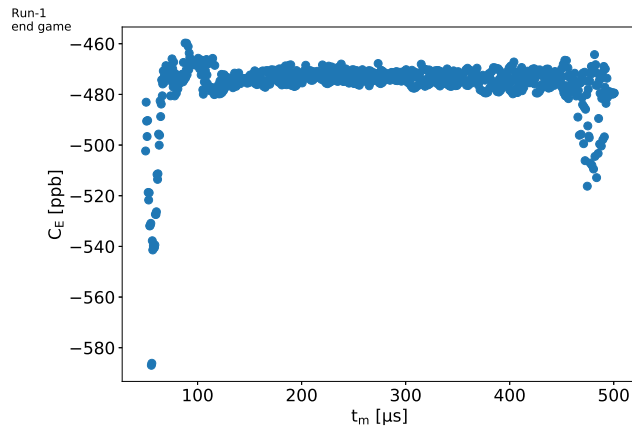
As explained in [1] Sec. 7.3 and [2] Sec. 4.2, there is a trade-off increasing the length of the fast rotation signal between improving the resolution and adding increasing noise. The interest of performing a t_m scan is to optimize this trade-off. Figure 26 shows the fast rotation analysis results as a function of t_m for t_s fixed to $t_s = 4 \mu s$. Figure 27 shows the same information but for $t_m > 150 \mu s$. For each t_m value, the analysis is performed with its nominal configuration. Figure 28 shows the background fit residuals and χ^2 per degrees of freedom as a function of t_m . Figure 29 shows the same information but for $t_m > 150 \mu s$. Overall, the results appear the most stable for t_m values between 150-300 μs . Before 150 μs , the resolution is too low and leads to a poor fidelity of the frequency distribution. After 300 μs , the increasing statistical noise of the fast rotation signal (see Fig. 3(f)) distorts the cosine Fourier transform. Figure 30 shows the background fit to the cosine Fourier transform for six values of t_m . The systematic uncertainty is taken as half the maximum variation of the results between 150 and 300 μs . The variation in the results might mainly be due to spectral leakage given the small size of the statistical uncertainty and the very high statistical correlation between consecutive scan data points.



(a)

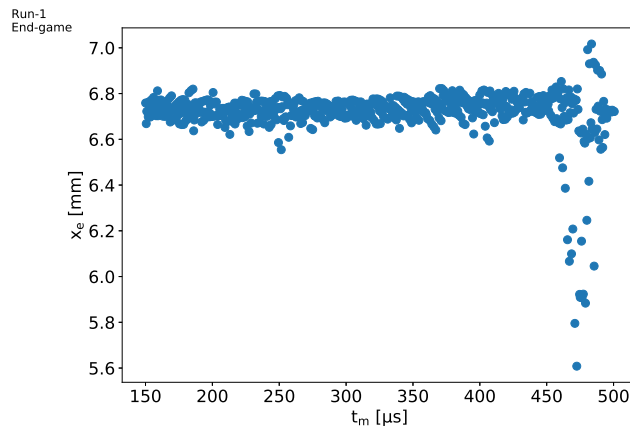


(b)

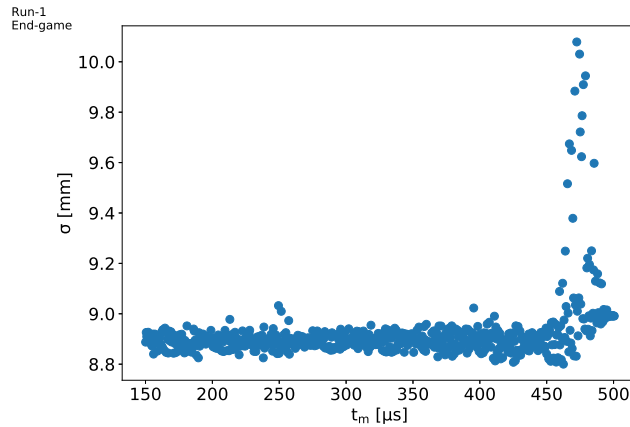


(c)

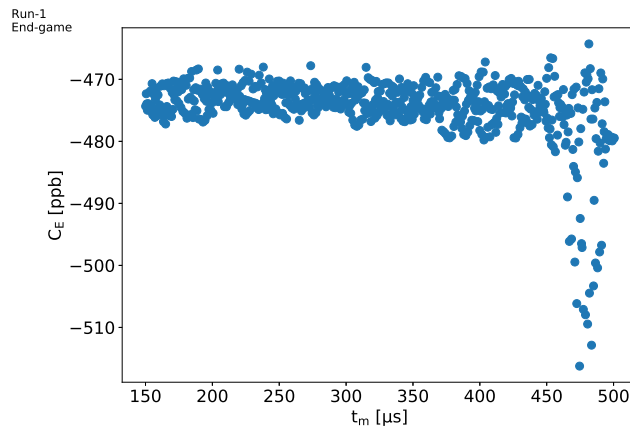
Figure 26: Results of the fast rotation analysis for $t_s = 4 \mu\text{s}$ as a function of t_m : (a) x_e , (b) σ , and (c) C_E .



(a)

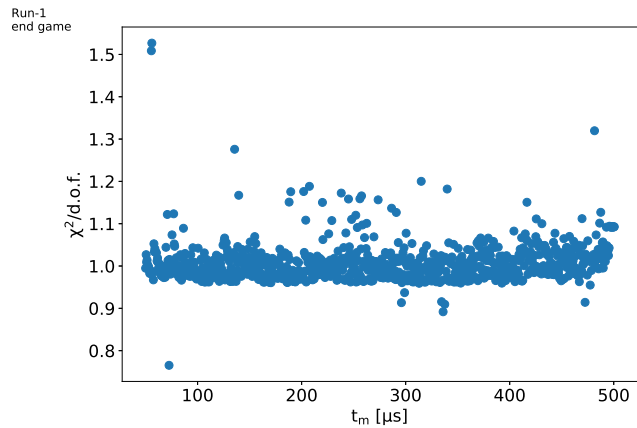


(b)

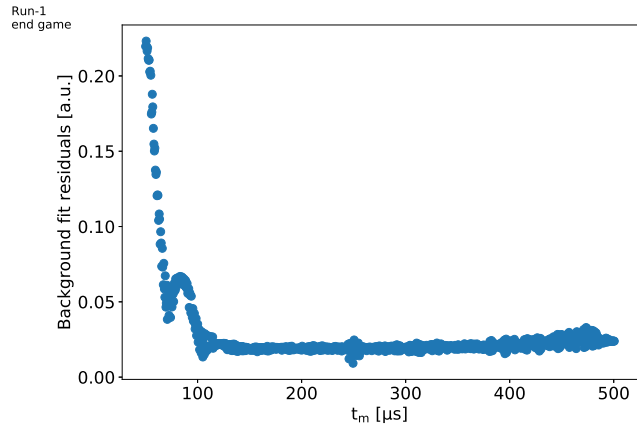


(c)

Figure 27: Results of the fast rotation analysis for $t_s = 4 \mu s$ as a function of t_m for $t_m > 150 \mu s$: (a) x_e , (b) σ , and (c) C_E .

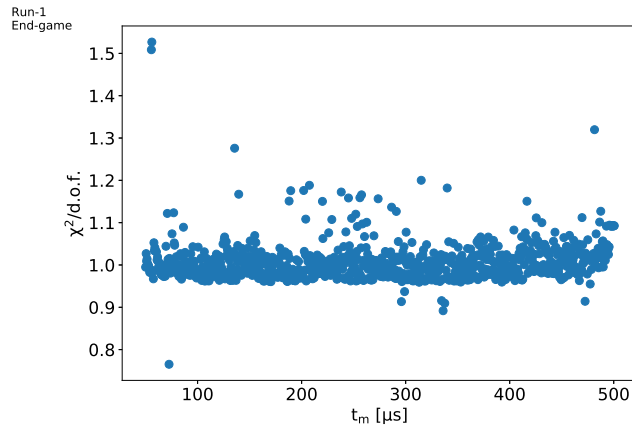


(a)

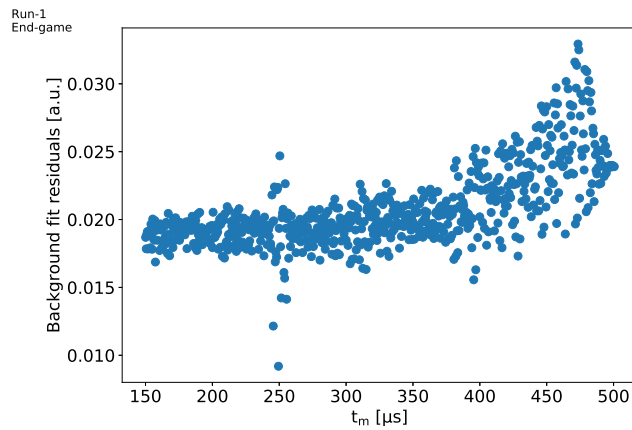


(b)

Figure 28: Background fit quality as a function of t_m : (a) $\chi^2/\text{d.o.f.}$, and (b) fit residuals.



(a)



(b)

Figure 29: Background fit quality as a function of t_m for $t_m > 150 \mu\text{s}$: (a) $\chi^2/\text{d.o.f.}$, and (b) fit residuals.

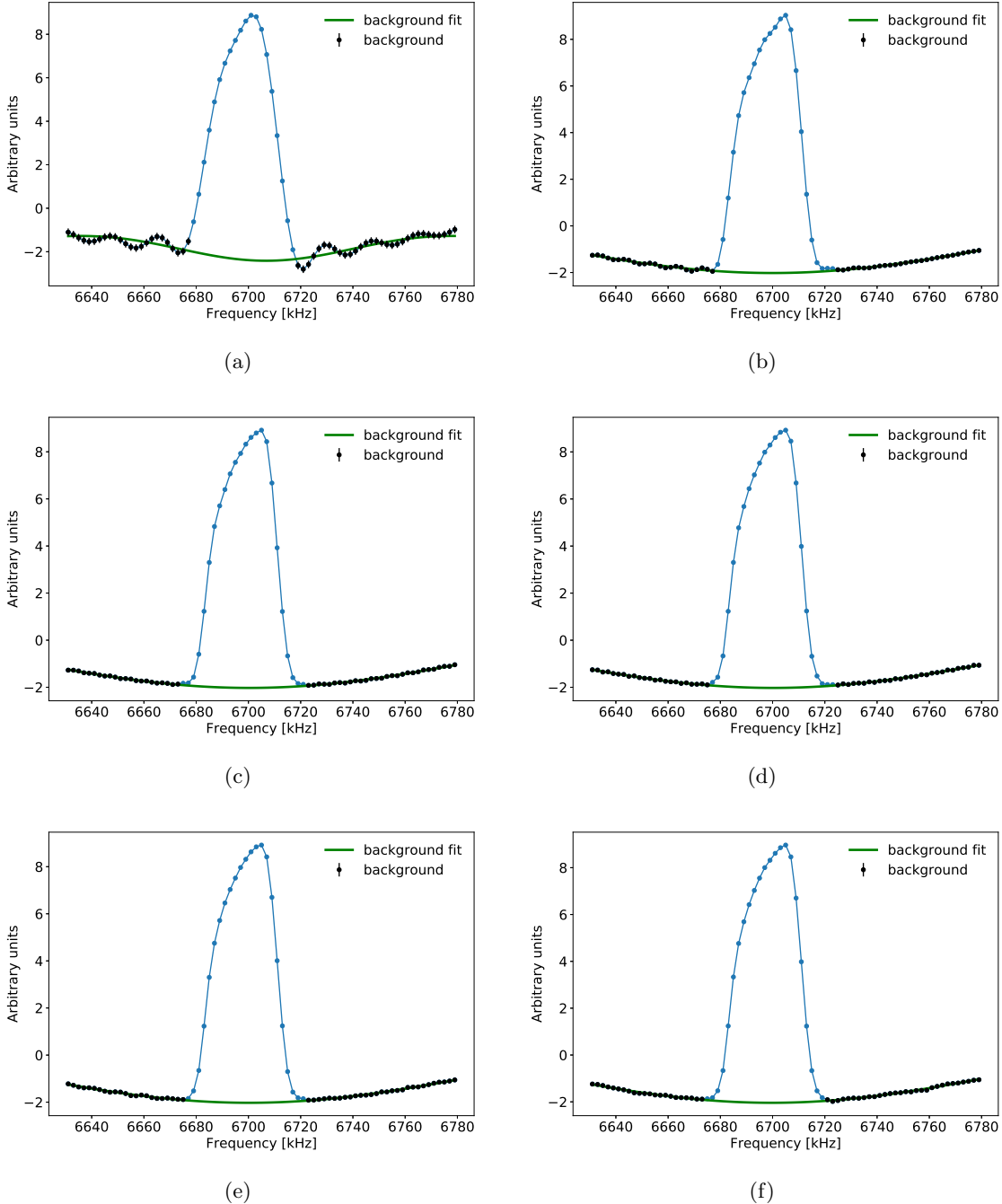


Figure 30: Background fit to the cosine Fourier transform for different t_m values: (a) 50, (b) 100, (c) 150, (d) 200, (e) 400, and (f) 500 μs .

7.4 Frequency interval

As explained in [1] Sec. 7.3 and [2] Sec. 4.4, the nominal frequency interval used to produce the cosine Fourier transform is 2 kHz. This 2 kHz value is smaller than the intrinsic frequency resolution that is set by the number of bins and time interval of the fast rotation signal. For $t_s = 4 \mu s$, $t_m = 300 \mu s$, and a 1 ns time interval, the intrinsic frequency resolution is:

$$1/(\text{time interval} \times \text{number of bins}) = 1/(10^{-9} \times 296000) = 3.34 \text{ kHz}.$$

Using a frequency interval of 2 kHz leads to over-sampling responsible for the modulation seen in Fig. 30(a) for instance. Over-sampling was shown in toy Monte Carlo studies (see [2] Sec. 4.4) to be sound. Nonetheless, a frequency interval scan is performed to ensure the same behavior in data. Figure 31 shows the fast rotation results as a function of frequency interval. The allowed values for the frequency interval are integer numbers of the frequency window used for the cosine Fourier transform. The results appear stable for a frequency interval up to 2.5 kHz. This behavior is the same as the one observed in the toy Monte Carlo studies (see [2] Sec. 4.4). The systematic uncertainty is taken as half the maximum variation in the results for the upper limit of the frequency interval of 2.5 kHz. Above 2.5 kHz, the fidelity of the frequency/radial distribution cannot be restored well enough due to the small number of data points.

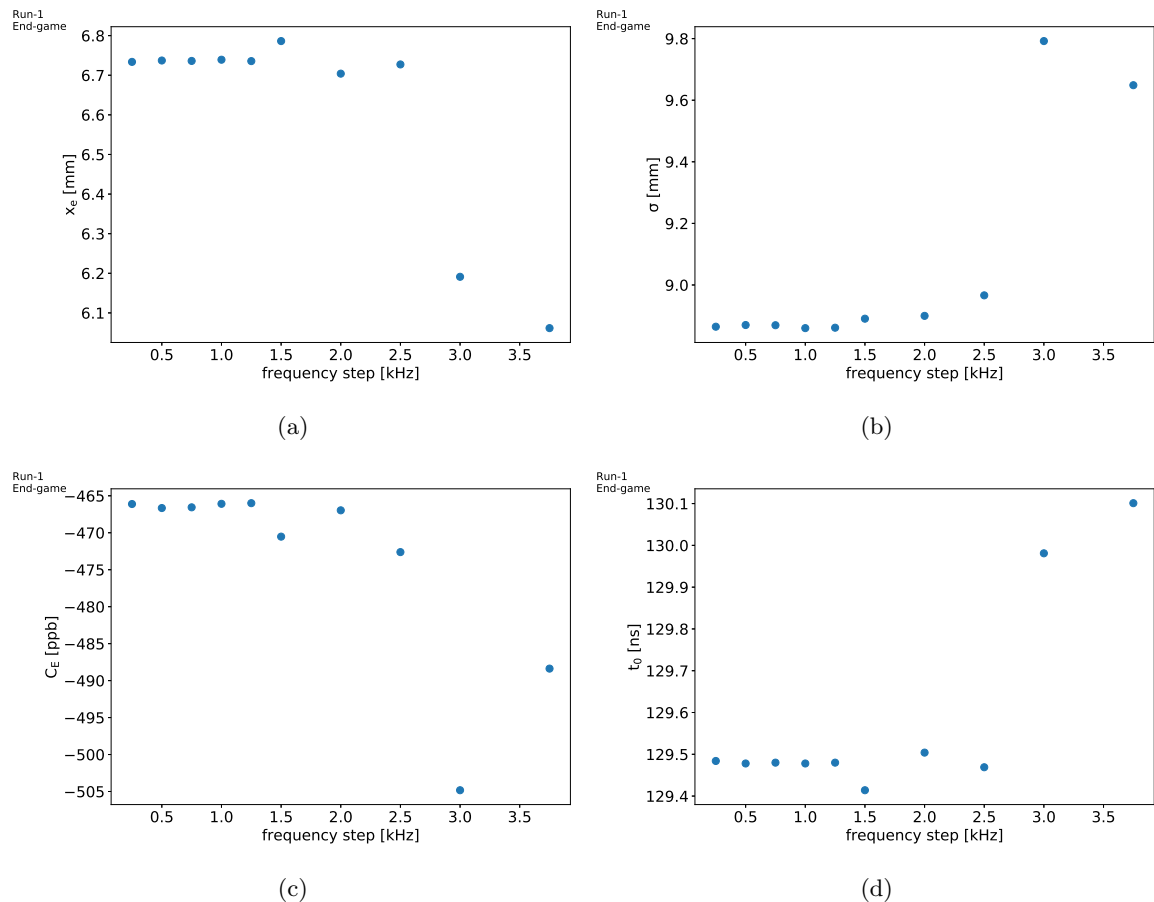


Figure 31: Results of the fast rotation analysis as a function of the frequency interval: (a) x_e , (b) σ , and (c) C_E .

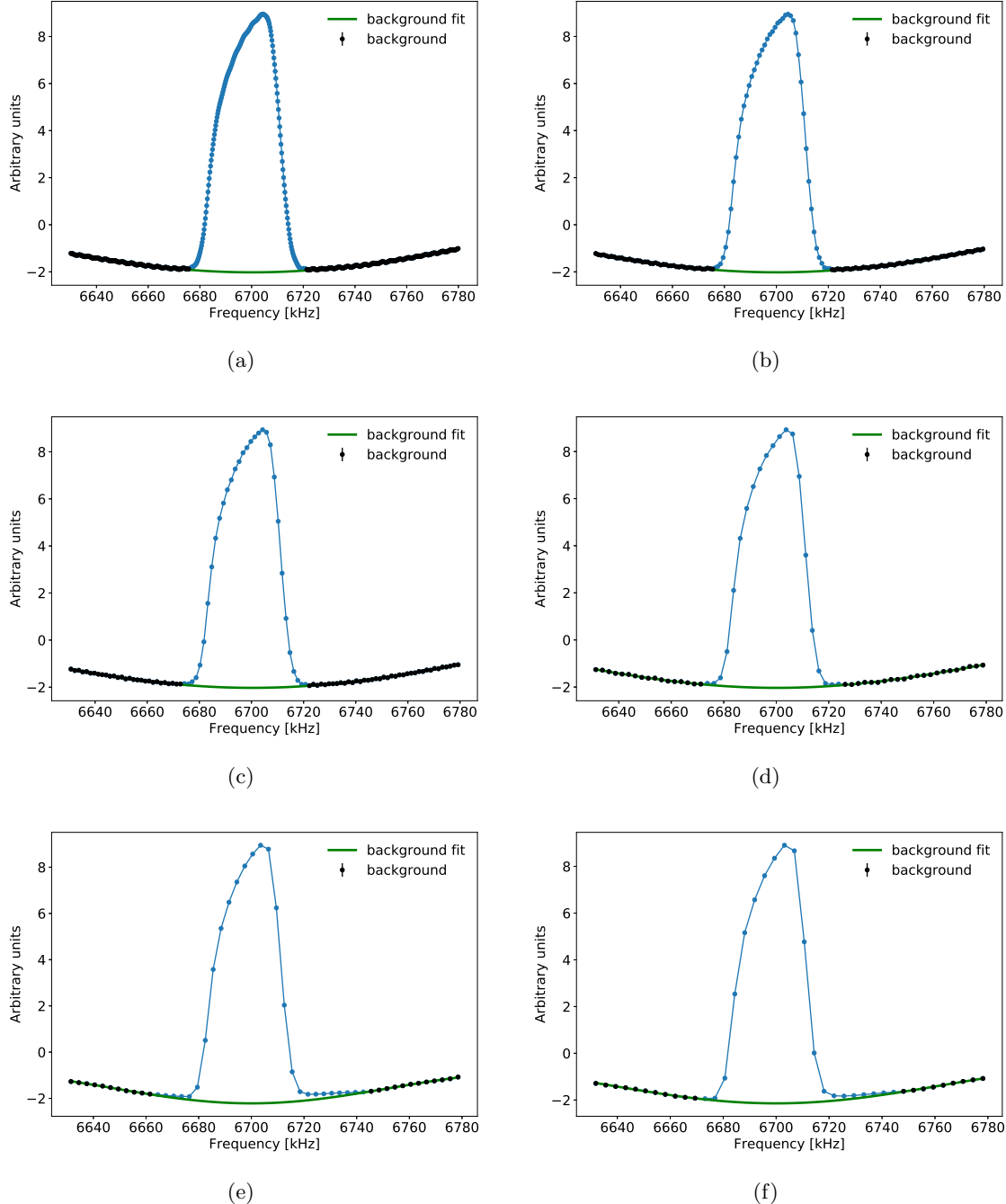


Figure 32: Background fit to the cosine Fourier transform for different frequency interval values: (a) 0.25, (b) 1.0, (c) 1.5, (d) 2.5, (e) 3.0, and (f) 3.75 kHz.

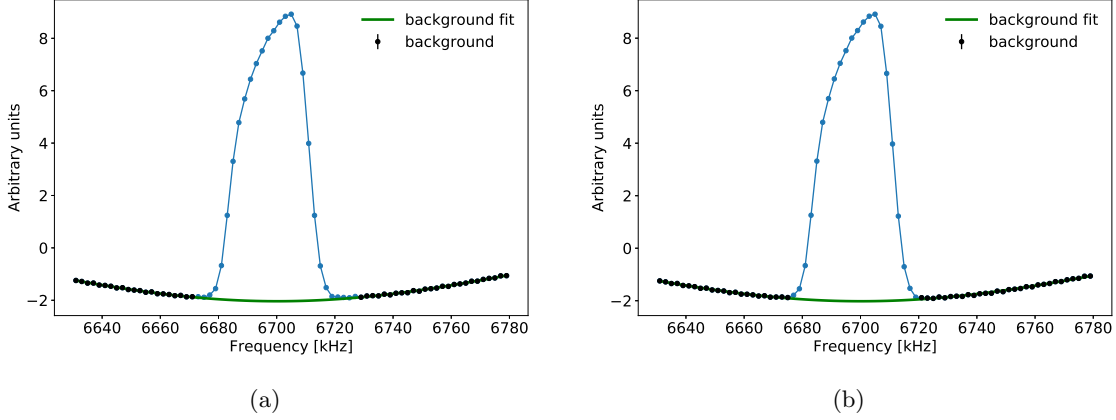


Figure 33: Background fit to the cosine Fourier transform for two background definition thresholds: (a) $N = 1$, and (b) $N = 5$.

7.5 Background

The definition of the background is key for optimizing t_0 and correcting the cosine Fourier transform. The functional form of the background is already part of the t_0 systematic uncertainty. The other sources of uncertainty from the background have to do with how it is defined, and how its statistical fluctuation can affect the analysis results via a lever arm effect, the data point being far from the mean of the distribution.

7.5.1 Background definition

The background of the cosine Fourier transform is defined as the data point that are within $\pm N \cdot \sigma_{bkg}$ of the fit with σ_{bkg} being the statistical noise of the background estimated from the fit residuals for the optimal t_0 value. The parameter that can be varied is N , its nominal value being $N = 2$. The larger N the closer to the mean of the distribution the background will get. Figure 33 shows the background fit for two values of N : $N = 1$ and $N = 5$. Figure 34 shows the results of the background threshold scan. Similarly to what is observed in toy Monte Carlo studies (see [2] Sec. 4.5), the width of the radial distribution decreases with N increasing. It is due to the fact that the background definition moves closer to the mean of the distribution for increasing N . It results in the background fit to be slightly shifted upward to account for the extra background data points, and therefore the corrected frequency distribution is shifted downward slightly, reducing the width in consequence. The systematic uncertainty is taken as half the maximum variation observed in the scan results.

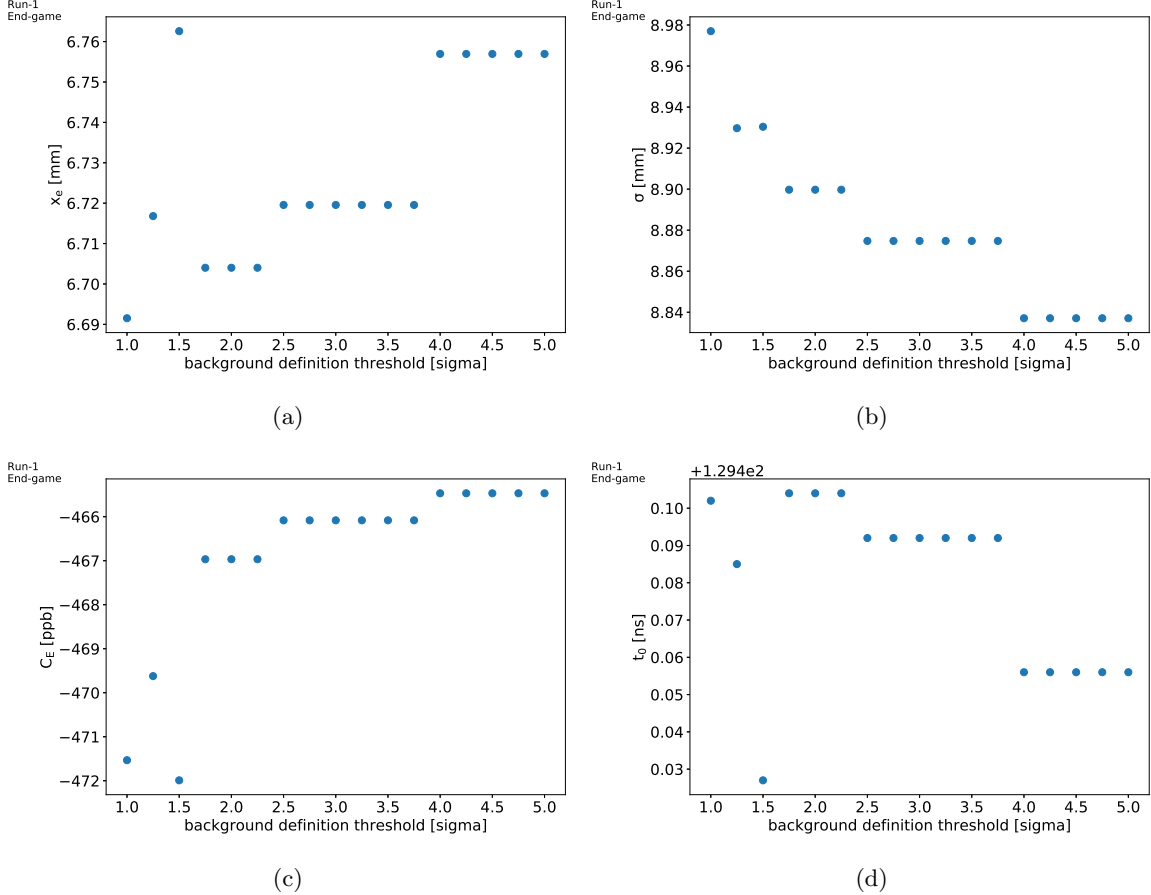


Figure 34: Results of the fast rotation analysis as a function of the background threshold definition N : (a) x_e , (b) σ , (c) C_E , and (d) t_0 .

7.5.2 Background removal

The statistical fluctuation in the tail (background) of the radial distribution can bias the extraction of the equilibrium radius and width given a potential large lever arm effect. This effect is addressed by removing (zero-ing out) the background from the distribution. The nominal fast rotation analysis is performed once with $N = 2$. The value of N is then varied and the data point within $\pm N \cdot \sigma_{bkg}$ of the nominal fit function (i.e. the data point tagged “background”) are removed. Figure 35 shows the radial distributions for $N = 1, 5$ with background removal. Figure 36 shows the results of the background removal scan. The systematic uncertainty is taken as half the maximum variation observed in the scan results.

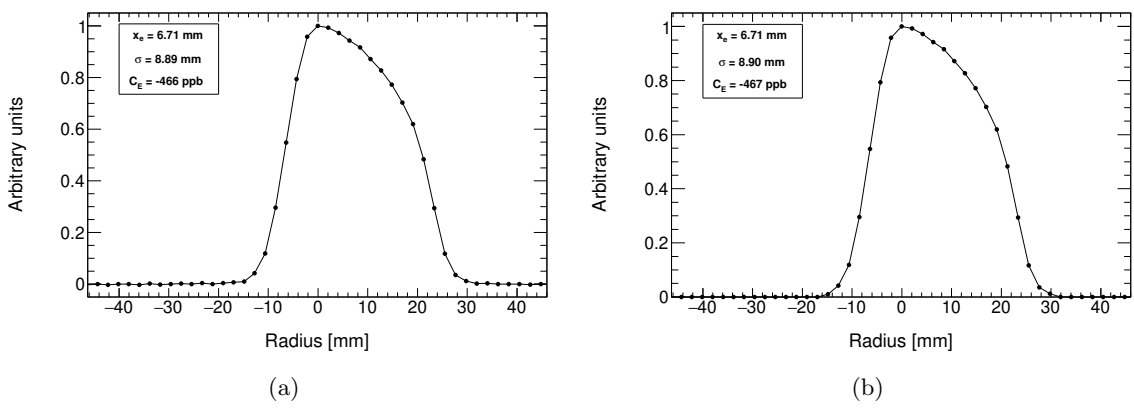
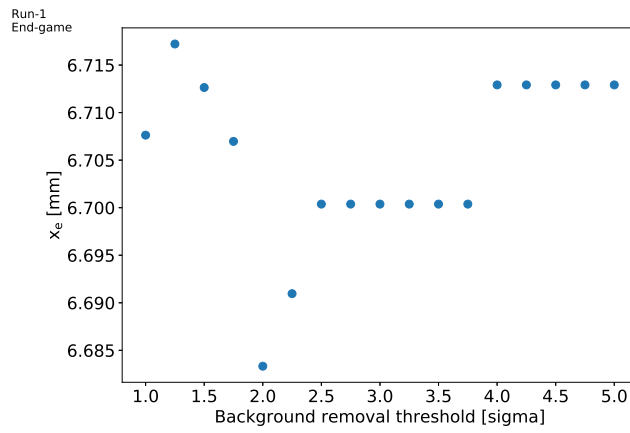
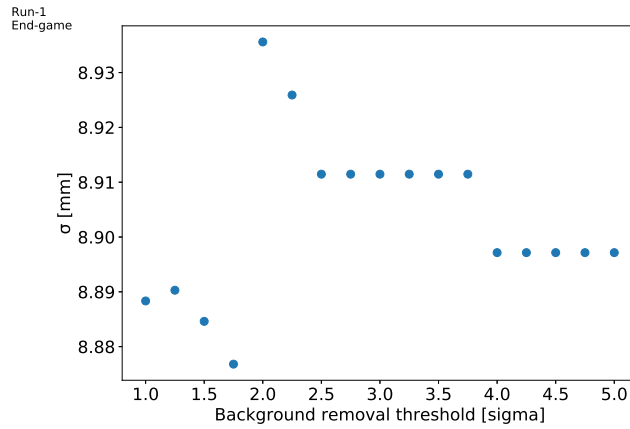


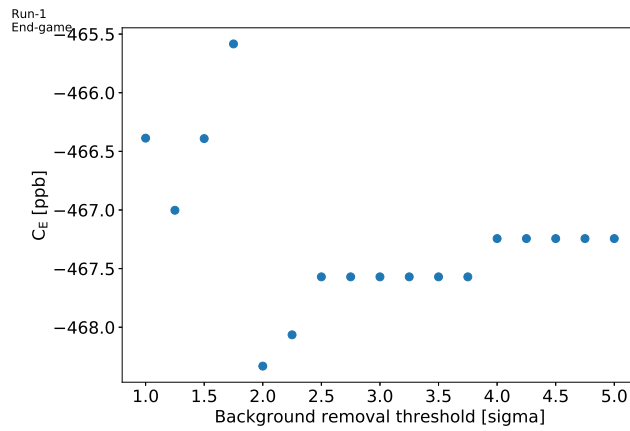
Figure 35: Radial distribution with background removal for: (a) $N = 1$, and (b) $N = 5$.



(a)



(b)



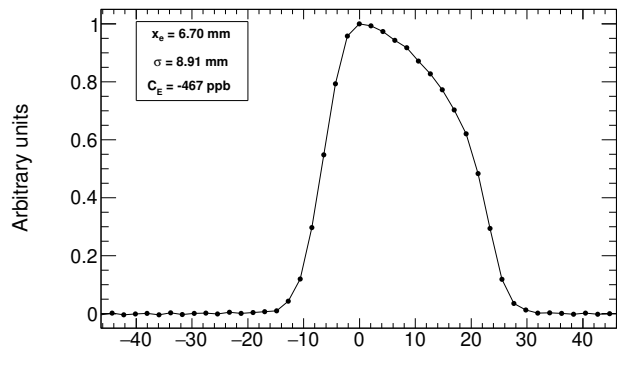
(c)

Figure 36: Results of the fast rotation analysis as a function of the background removal threshold N : (a) x_e , (b) σ , and (c) C_E .

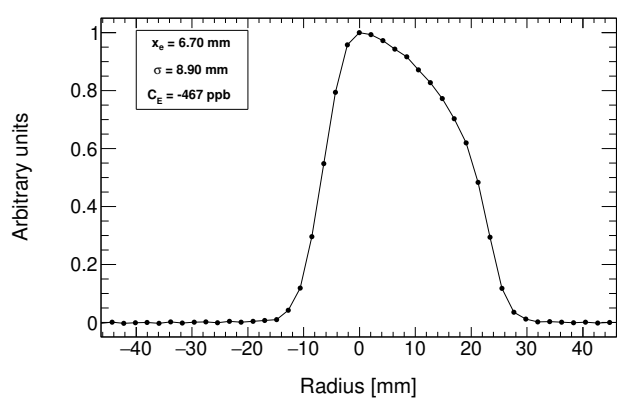
7.6 Wiggle fit

The nominal fit to the positron counts histogram is the 9-parameter fit: muon life-time, anomalous spin precession and CBO modulation. The anomalous spin precession frequency performs a fit to the positron counts histograms with many more parameters: pile-up, vertical waist, muon loss etc. In order to estimate the importance of the accuracy of the fit to the data, the analysis is performed on fast rotation signals produced using a different number of parameters in the wiggle fit: 2 (muon life-time only), 5 (muon life-time and anomalous spin precession) and 9 (muon life-time, anomalous spin precession and CBO modulation). Figure 37 shows the radial distribution for the three cases. The results appear to be consistent within the statistical uncertainty. This is not surprising because both the anomalous spin precession and CBO modulation frequencies (and their beating/aliasing frequencies) are not overlapping with the frequency range of the cyclotron revolution. It is important to note that fitting at least for the muon life-time is essential to avoid the artificial broadening of the cyclotron frequency peak due to the exponential decay in the fast rotation spectrum⁶. One question remains: what of the potential effects of pile-up, muon loss and gain correction not included in the fit? The t_s scan provides a good handle on it because the size of the pile-up, muon loss and gain correction effects significantly decreases over the first $30 \mu\text{s}$ of the fill and therefore are part of the systematic uncertainty associated with the t_s scan.

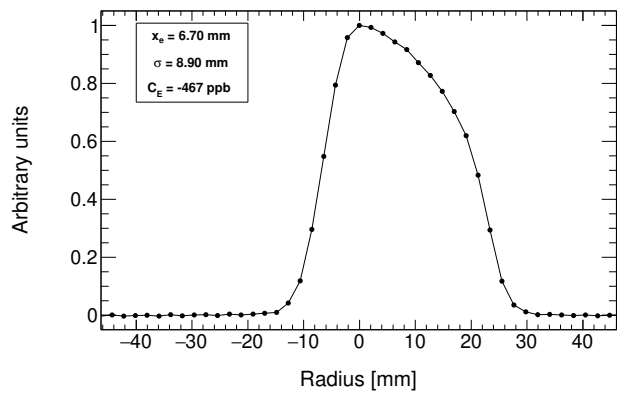
⁶The fast rotation exponential feature will enter the Fourier transform calculation and will yield a frequency broadening.



(a)



(b)



(c)

Figure 37: Radial distributions for fast rotation signals produced from a wiggle fit with:
 (a) 2 parameters, (b) 5 parameters, and (d) 9 parameters.

7.7 Positron energy threshold

The nominal positron energy threshold used to produce the positron counts histogram is 1,500 MeV. Given the anomalous spin precession frequency analysis is performed for different energy threshold values and with different methods (T-method, A-method, E-method, Q-method etc.), it is important to perform the fast rotation analysis as a function of the energy threshold. The nominal fast rotation analysis is therefore performed⁷ for positron counts histograms produced with a wide range of positron energy threshold. Appendix D shows fast rotation histograms for different positron energy thresholds. Figure 38 shows the results of the fast rotation analysis as a function of the positron energy threshold. The statistical uncertainty on each data point is not shown, but increases with increasing energy threshold. There is a clear trend of x_e and σ increasing with the energy threshold. This effect is believed to be related to a calorimeter acceptance effect, and not to a beam dynamics effect. It needs to be thoroughly studied with full scale high statistics simulations with BMAD and GM2RINGSIM. The value of the systematic uncertainty is taken as half the maximum variation and is under control for this Run–1 data set.

⁷The only exception being the background definition being fixed to avoid the associated systematic effect.

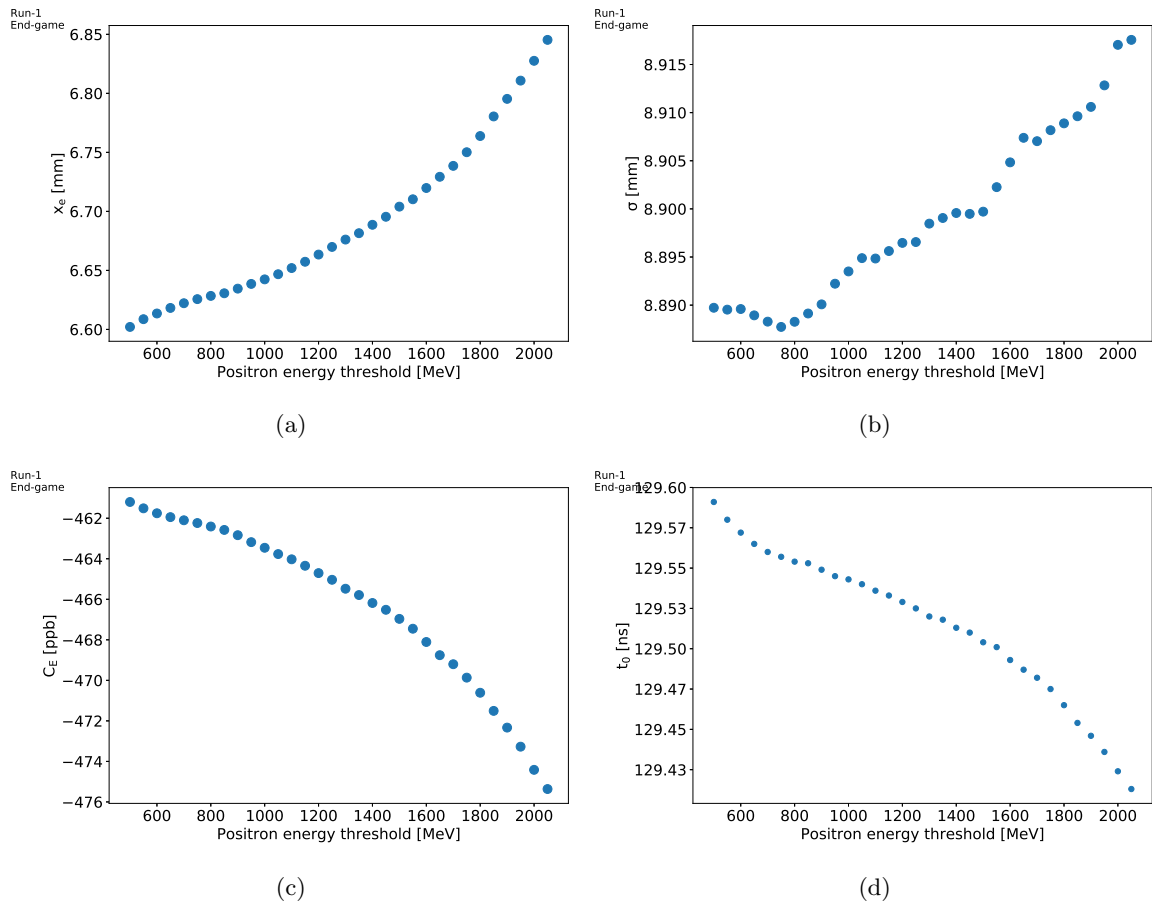


Figure 38: Results of the fast rotation analysis as a function of the positron energy threshold: (a) x_e , (b) σ , (c) C_E , and (d) t_0 .

	t_0 [ns]	x_e [mm]	σ [mm]	C_E [ppb]
t_0	0.02	0.01	0.01	1
t_s	–	0.07	0.03	3
t_m	0.14	0.13	0.10	5
$t_0 \pm T_c$	–	0.02	0.05	3
frequency interval	0.05	0.04	0.05	3
background definition	0.04	0.04	0.07	3
background removal	–	0.02	0.03	1
wiggle fit	0.01	0.01	0.01	1
energy threshold	0.10	0.13	0.15	8
systematic (0% correlation)	0.19	0.21	0.21	11
systematic (100% correlation)	0.36	0.49	0.50	28

Table 5: Summary of the estimation of the systematic uncertainties and the total uncertainty assuming 0% and 100% correlation..

7.8 Summary

The correlation between the various systematic uncertainties has not been estimated. Table 5 summarizes the estimation of the various systematic uncertainties and the corresponding total assuming 0% correlation (quadratic sum) and 100% of correlation (linear sum) between all the systematic uncertainties. The final systematic uncertainty numbers are taken as the average of the 0% and 100% correlation cases.

8 Conclusion

The final results of the fast rotation analysis of the Run–1 End–game data set data set is:

$$\begin{aligned} x_e &= 6.70 \pm 0.01 \text{ (stat)} \pm 0.35 \text{ (syst)} \text{ mm,} \\ \sigma &= 8.90 \pm 0.01 \text{ (stat)} \pm 0.36 \text{ (syst)} \text{ mm,} \\ C_E &= -467 \pm 1 \text{ (stat)} \pm 20 \text{ (syst)} \text{ ppb.} \end{aligned}$$

The level of uncertainty is satisfying for the Run–1. There is room, however, to improve the uncertainty by bettering the understanding of the analysis performance and impacts from beam dynamics and detector effects. It will rely on thorough studies with toy Monte Carlo, BMAD and GM2RINGSIM. The main uncertainty to be tackled are related to the start and end time scans, as well as the positron energy threshold. It is possible that additional

systematic uncertainties will be estimated in the future: time-momentum correlation of the incoming bunch, muon loss, etc. (see [2] Sec. 5). The correlations between the various systematic uncertainties need to be estimated for a more accurate estimation of the total systematic uncertainty⁸. The approach of estimating a systematic uncertainty by taking half the maximum variation in the results for a given systematic scan could also be revisited, taking the spread in the results is an alternate approach.

These questions leave room to improve the uncertainty by bettering the understanding of the analysis performance and impacts from beam dynamics and detector effects. It will rely on thorough studies with toy Monte Carlo, BMAD and GM2RINGSIM. It is possible that additional systematic uncertainties will be estimated in the future: time-momentum correlation of the incoming bunch, muon loss, etc. (see [2] Sec. 5). The correlations between the various systematic uncertainties need to be estimated for a more accurate estimation of the total systematic uncertainty⁹. The approach of estimating a systematic uncertainty by taking half the maximum variation in the results for a given systematic scan could also be revisited, taking the spread in the results is an alternate approach.

This will not happen for Run–1 but will hopefully happen for the Run–2 analysis. Improvements for Run–2 are expected using the information provided by the IBMS3 detector. The IBMS3 detector can measure the beam profile for the first μs after injection starting from injection itself. It will likely prove useful.

Important: the uncertainties above are associated with the fast rotation analysis itself. It needs to be added the uncertainty associated with the simulation efforts led by David Rubin. The work aims at estimating the uncertainty on the electric correction due to the uncertainty on the electrostatic quadrupoles plate alignment, voltages etc. The final number on the electric field correction is currently:

$$C_E = -463 \pm 20 \text{ (fast rotation analysis)} \pm ?? \text{ (simulation) ppb.}$$

References

- [1] A. Chapelain, J. Fagin, D. Rubin, D. Seleznev, *Cornell fast rotation Fourier method*, [GM2-doc-18901](#)
- [2] A. Chapelain, J. Fagin, D. Rubin, D. Seleznev, *Performance study of the Cornell fast rotation Fourier analysis with toy Monte Carlo simulations*, [GM2-doc-19132](#)

⁸It means the current total uncertainty budget might be over- or under-estimated depending on what the correlations actually are.

⁹It means the current total uncertainty budget might be over- or under-estimated depending on what the correlations actually are.

- [3] A. Chapelain, D. Rubin, D. Seleznev, *Extraction of the Muon Beam Frequency Distribution via the Fourier Analysis of the Fast Rotation Signal*, E989 note 130, [GM2-doc-9701](#)
- [4] A. Chapelain, J. Fagin, D. Rubin, D. Seleznev, *On the background correction of the Cornell fast rotation Fourier method*, [GM2-doc-19225](#)
- [5] A. Chapelain, J. Fagin, D. Rubin, D. Seleznev, *Cornell fast rotation Fourier analysis user guide*, [GM2-doc-18460](#)
- [6] See [Production Run-1 data wiki](#)
- [7] A. Fienberg, *Global T0 study*, [GM2-doc-18964](#)
- [8] See ‘TMC #1’ in: [GM2-doc-13759](#)
- [9] See ‘TMC #3’ in: [GM2-doc-13759](#)
- [10] A. Chapelain, J. Fagin, D. Rubin, D. Seleznev, *Fast rotation analysis of the Run-1 60-hour data set with the Cornell Fourier method*, [GM2-doc-19150](#)
- [11] A. Chapelain, J. Fagin, D. Rubin, D. Seleznev, *Fast rotation analysis of the Run-1 9-day data set with the Cornell Fourier method*, [GM2-doc-19252](#)

A Fast rotation histogram per-bunch

Figure 39 shows the fast rotation histograms between 4 and 5 μs after injection for the 8 individual accelerator bunches.

B Fast rotation histogram per-calorimeter

Figures 40, 41 and 42 show the fast rotation histograms between 4 and 5 μs after injection for the 24 individual calorimeters.

C Wiggle fit residuals

Figure 43 shows the wiggle fit residuals for different time windows with the common lower value being the start time of the fit of 30 μs . The residuals, as expected, are not randomly distributed according to the statistical uncertainty. The residuals exhibit clear features. These features are due to missing ingredients in the fit: vertical waist modulation, muon loss, gain correction, pile-up etc.

Figure 44 shows the wiggle fit residuals for the time window 4-31 μs . The residuals exhibit features with larger amplitude. The main one is due to the CBO modulation. The CBO frequency changes over the course of the first 30 μs due to scraping and thus is not properly modeled for a fit start time of 30 μs with a fitted constant CBO frequency.

D Fast rotation histogram for different positron energy thresholds

Figure 45 shows the fast rotation signal between 4-5 μs after injection for different positron energy thresholds.

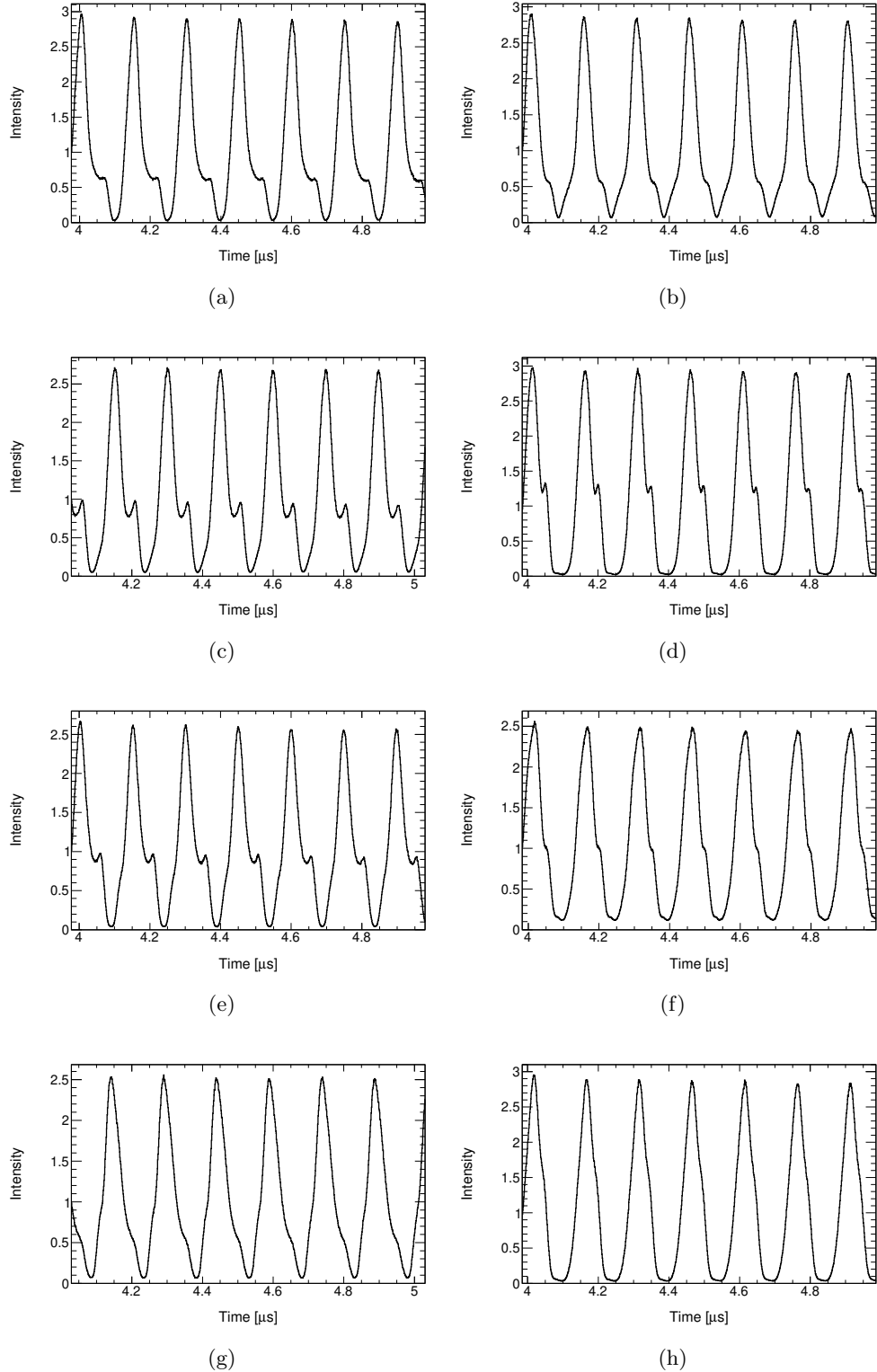


Figure 39: Fast rotation histograms from 4 to 5 μs after injection for the 8 accelerator bunches: (a) to (h) are respectively bunches #0 to #7.

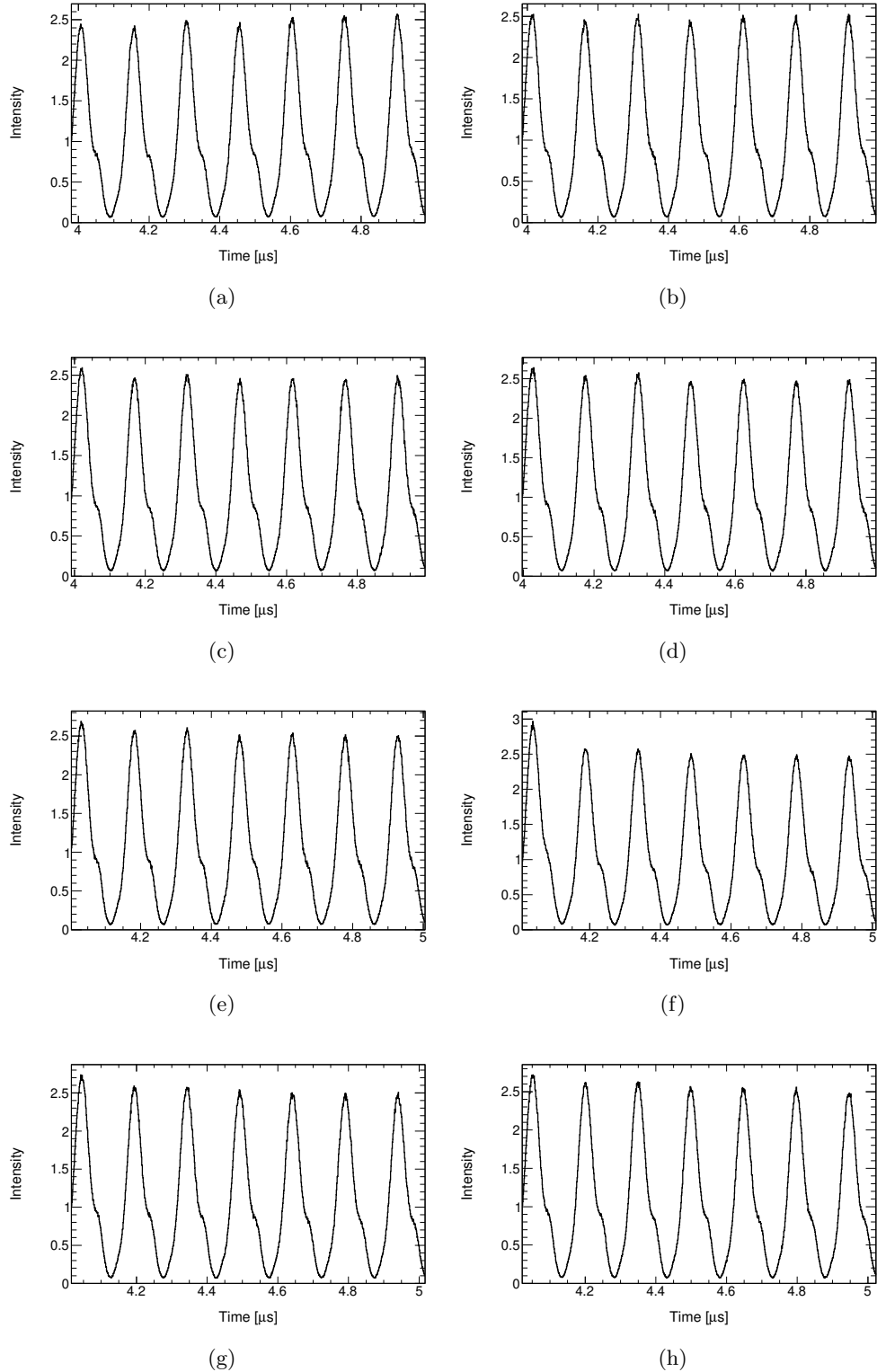


Figure 40: Fast rotation histograms from 4 to 5 μs after injection for 8 calorimeters: (a) to (h) are respectively calorimeter #1 to #8.

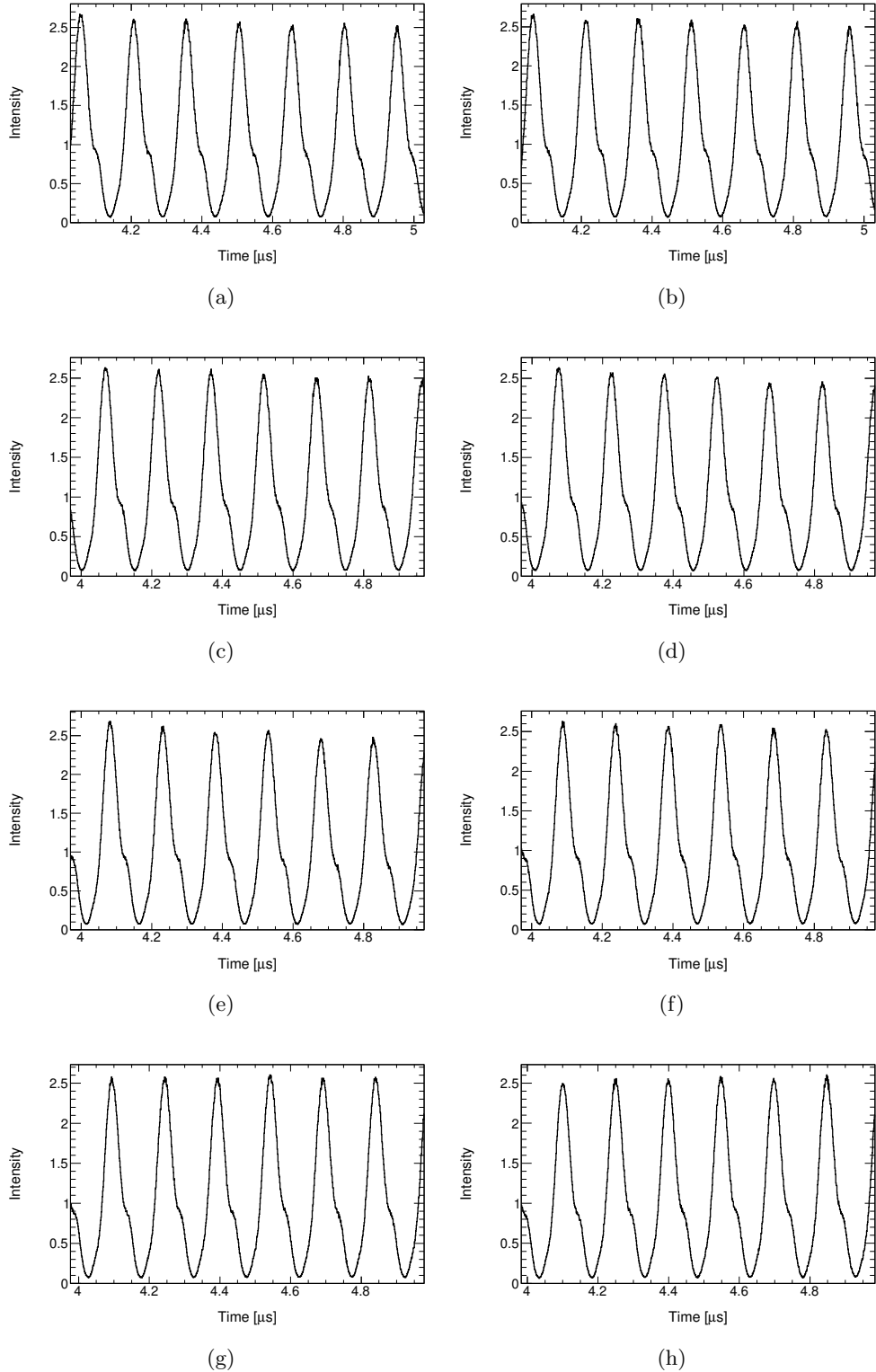


Figure 41: Fast rotation histograms from 4 to 5 μs after injection for 8 calorimeters: (a) to (h) are respectively calorimeter #9 to #16.

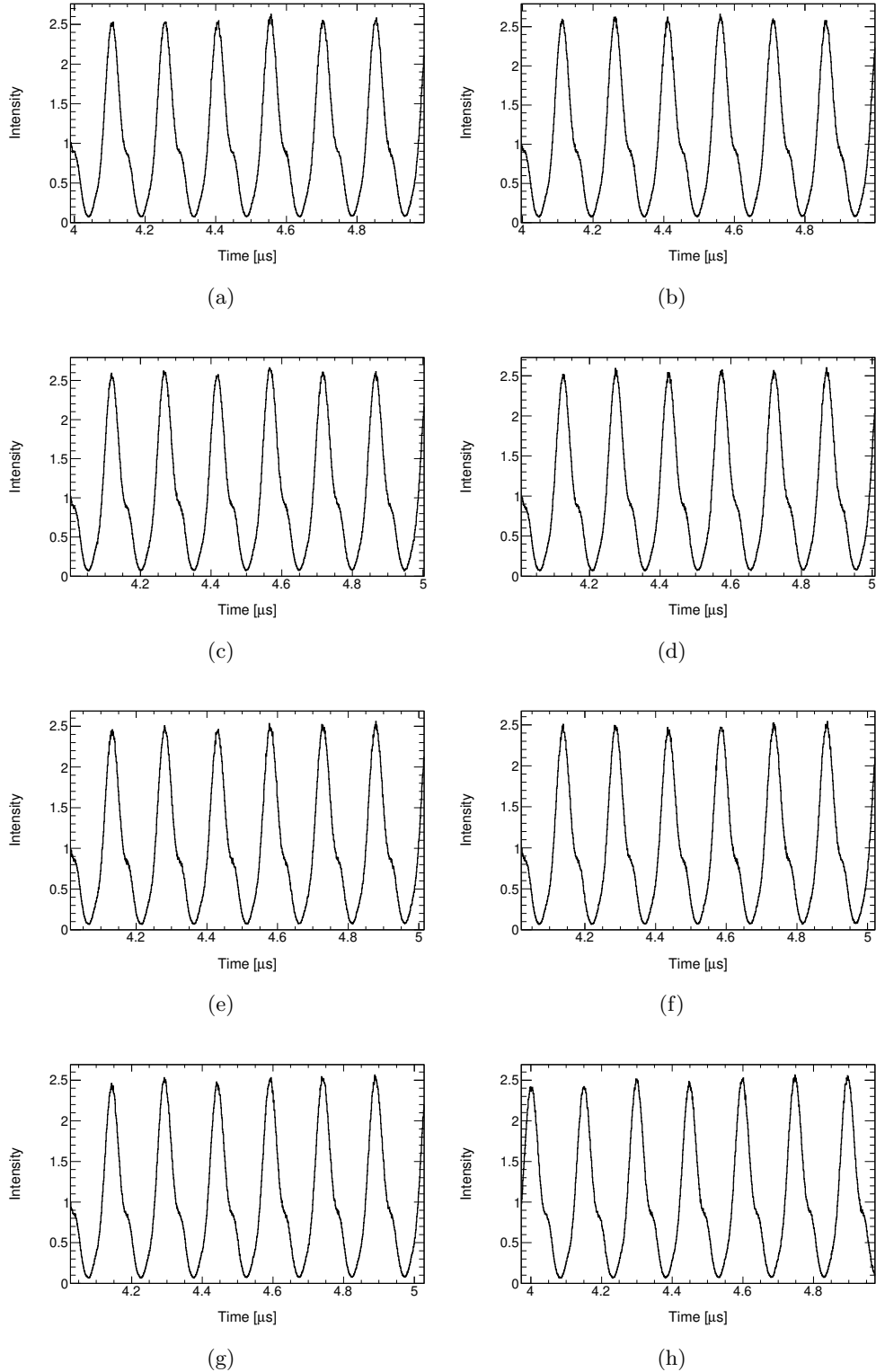


Figure 42: Fast rotation histograms from 4 to 5 μs after injection for 8 calorimeters: (a) to (h) are respectively calorimeter #17 to #24.

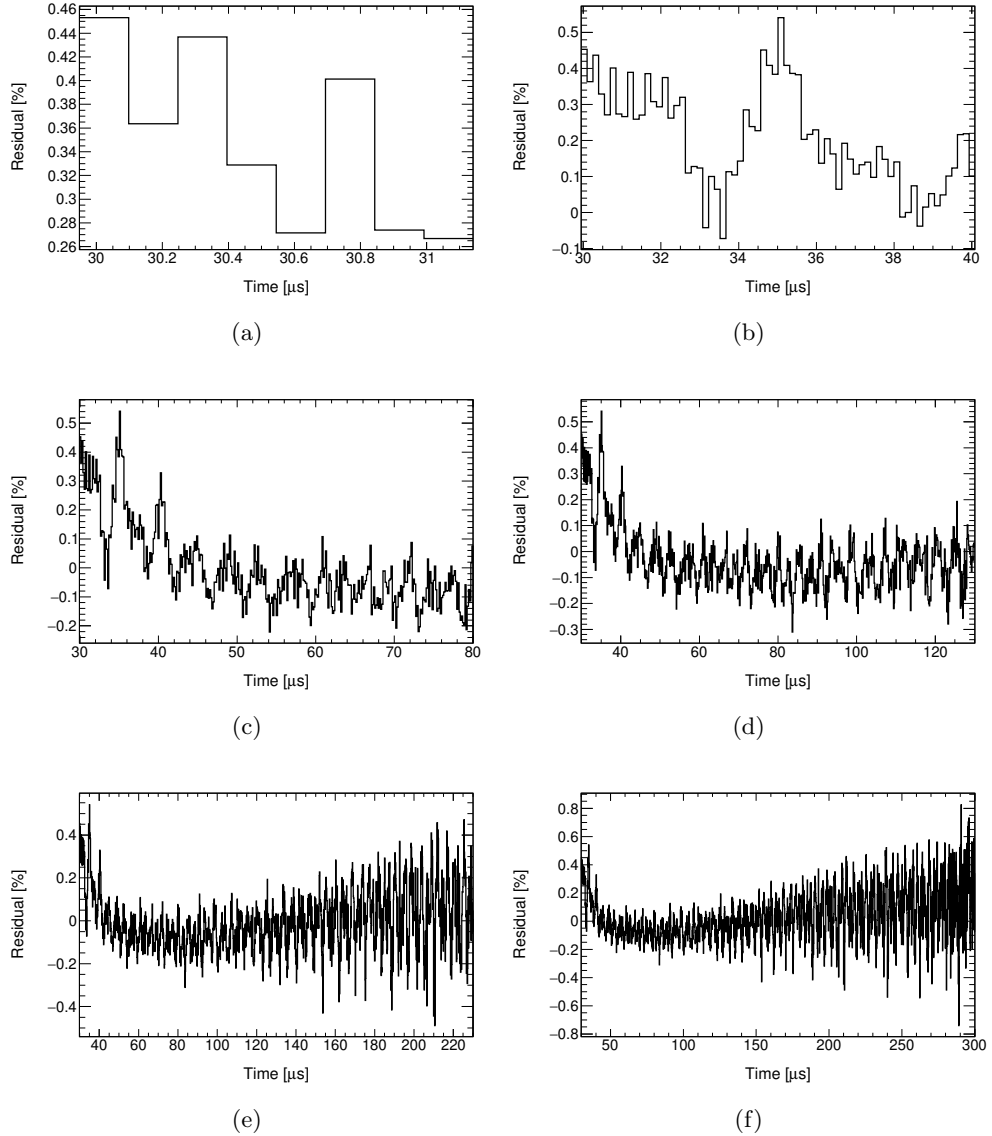


Figure 43: Residuals of the 9-parameter wiggle fit for six different time window: (a) 30-31, (b) 30-40, (c) 30-80, (d) 30-130, (e) 30-230 and (f) 30-300 μs . The start time of the fit is 30 μs .

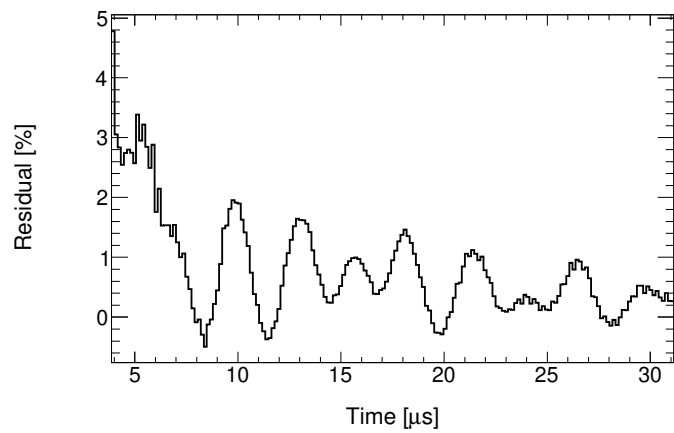


Figure 44: Residuals of the 9-parameter wiggle fit for the time window 4-31 μ s. The start time of the fit is 30 μ s.

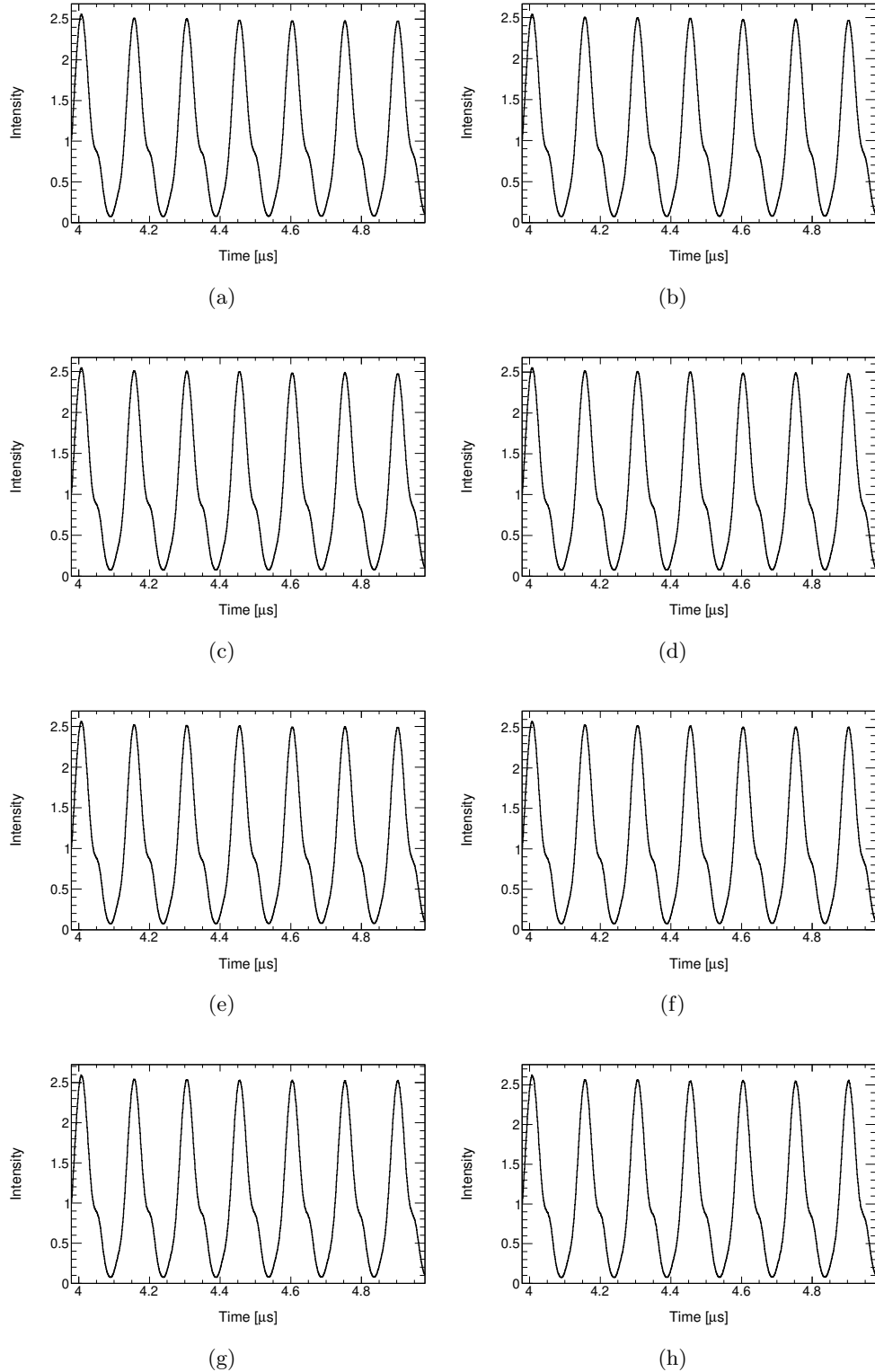


Figure 45: Fast rotation histograms from 4 to 5 μs after injection for 8 positron energy thresholds: (a) 500, (b) 700, (c) 900, (d) 1100, (e) 1300, (f) 1500, (g) 1700, and (h) 1900 MeV.